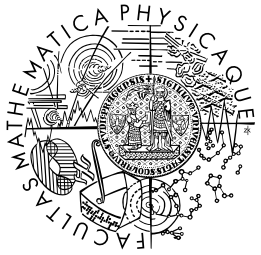

FACULTY
OF MATHEMATICS
AND PHYSICS
Charles University

MASTER THESIS

Ondřej Zelenka

Dynamics of spinning test particles in curved spacetimes

Institute of Theoretical Physics

Supervisor of the master thesis:	Georgios Loukes Gerakopoulos, Ph.D.
Study programme:	Physics
Study branch:	Theoretical Physics

Prague 2019

I declare that I carried out this master thesis independently, and only with the cited sources, literature and other professional sources.

I understand that my work relates to the rights and obligations under the Act No. 121/2000 Sb., the Copyright Act, as amended, in particular the fact that the Charles University has the right to conclude a license agreement on the use of this work as a school work pursuant to Section 60 subsection 1 of the Copyright Act.

In ..... date ..... signature of the author

I give great thanks to my supervisor Georgios Lukes-Gerakopoulos, who has guided me through this work, and to Vojtěch Witzany, who has been very helpful as well. I also express my gratitude to the Theoretical Physics Institute at the Friedrich-Schiller-Universität in Jena for their hospitality and to Sebastiano Bernuzzi, Enno Harms and Sarp Akcay for helpful discussions and comments.

This work was supported by Grant No. GAČR-17-06962Y of the Czech Science Foundation, which is acknowledged gratefully. I am grateful to the Astronomical Institute of the Czech Academy of Sciences, which has given me a workplace and together with Michal Bursa allowed and helped me to use the Virgo cluster to perform Teukode simulations.

Finally, I am grateful to my family and close ones, who have helped me and supported me through all problems, difficulties and compiler errors.

Title: Dynamics of spinning test particles in curved spacetimes

Author: Ondřej Zelenka

Institute: Institute of Theoretical Physics

Supervisor: Georgios Loukes Gerakopoulos, Ph.D.,
Astronomical Institute of the Czech Academy of Sciences

Abstract: The motion of a test particle in the Schwarzschild background models the merger of a compact object binary with extremely different masses known in the literature as Extreme Mass Ratio Inspiral. In the simplest geodesic approximation, this motion is integrable and there is no chaos. When one takes the spin of the smaller body into account, integrability is broken and prolonged resonances along with chaotic orbits appear. By employing the methods of Poincaré surface of section, rotation number and recurrence analysis we show for the first time that there is chaos for astrophysically relevant spin values. We propose a universal method of measuring widths of resonances in perturbations of geodesic motion in the Schwarzschild spacetime using action-angle-like variables. We apply this novel method to demonstrate that one of the most prominent resonances is driven by second order in spin terms by studying its growth, supporting the expectation that chaos will not play a dominant role in Extreme Mass Ratio Inspirals. Last but not least, we compute gravitational waveforms in the time-domain and establish that they carry information on the motion's dynamics. In particular, we show that the time series of the gravitational wave strain can be used to discern regular from chaotic motion of the source.

Keywords: black holes, spinning particles, chaos, gravitational waves

Název práce: Dynamika rotujících testovacích částic v zakřivených prostoročasech

Autor: Ondřej Zelenka

Ústav: Ústav teoretické fyziky

Vedoucí diplomové práce: Georgios Loukes Gerakopoulos, Ph.D., Astronomický ústav Akademie věd ČR

Abstrakt: Pohybem testovací částice ve Schwarzschildově prostoročase lze modelovat splynutí kompaktních objektů s extrémně rozdílnými hmotnostmi známé v literatuře jako Extreme Mass Ratio Inspiral. V nejjednodušší geodetické aproximaci je tento pohyb integrabilní a nedochází k chaotickému chování. Pokud se vezme v úvahu rotace menšího z těles, systém ztrácí integrabilitu a objeví se prodloužené rezonance a chaotické trajektorie. Použitím metod Poincarého řezu, rotačního čísla a rekurenční analýzy poprvé dokazujeme, že existuje chaos pro astrofyzikálně relevantní hodnoty momentu hybnosti. Navrhujeme univerzální metodu pro měření šířek rezonancí v perturbacích geodetického pohybu ve Schwarzschildově prostoročase použitím proměnných akce-úhel. Použitím této nové metody ukazujeme, že jedna z nejvýraznějších rezonancí vzniká díky členům druhého řádu v momentu hybnosti, studiem jejího růstu, což je v souladu s očekáváním, že chaos nebude hrát dominantní roli v Extreme Mass Ratio Inspiral. Také počítáme gravitační vlny v časovém oboru a nacházíme v nich informace o dynamice systému. Především dokazujeme, že časovou řadu deformace prostoročasu způsobené gravitačními vlnami lze použít k rozlišení regulárního a chaotického chování zdroje.

Klíčová slova: černé díry, rotující částice, chaos, gravitační vlny

Contents

Introduction

The last few years have witnessed the birth of gravitational wave astronomy. Although the first indirect evidence of gravitational waves has been known since the early 1980s [1], the first direct detection GW150914 by the LIGO Scientific Collaboration [2] has been celebrated around the globe and since then, ~ 10 more events have been detected [3]. All of them have been calculated to be mergers of compact binaries of comparable masses between $10^1 M_\odot$ and $10^2 M_\odot$.

The Laser Interferometric Space Antenna (LISA) mission, the first dedicated space-based gravitational wave detector, is expected to launch in 2034 [4]. Unlike ground-based detectors, the sensitivity of LISA will lie in the range from 10^{-4} Hz to 10^{-2} Hz, allowing for observation of many different types of sources such as supermassive black hole mergers [5] or stellar mass compact binaries long before merger [6]. Another exciting prospect is to use these sources as independent standard sirens that allow us to constrain cosmological models [7]. One of the primary targets are the inspirals of stellar mass ($10^0 M_\odot - 10^1 M_\odot$) compact objects (black holes or neutron stars) into supermassive black holes ($10^5\, M_\odot - 10^{10}\, M_\odot$), which are called Extreme Mass Ratio Inspirals (EMRIs). It is expected that after the mission has launched, LISA will detect between 1 and 2000 EMRIs per year [4].

The full description of a compact binary requires solving the full Einstein equations using numerical relativity simulations and constitutes a computationally expensive task. Indeed, the computational requirements in a crude estimate rise as the fifth power of the mass ratio. In the case of an EMRI, the computational cost is prohibitive. Fortunately, the dynamics of an EMRI can be modeled as the motion of an extended body in a perturbed black hole spacetime. The gravitational perturbation of the spacetime background is caused by the presence of the smaller body, and this effect ultimately drives the inspiral. However, the back-reaction that is induced on the motion of the small body itself accumulates very slowly, and it is meaningful to ignore it in the orbital dynamics for a certain period of time. As a result, we may study the effect of the finite size of the smaller object in a *test body* approximation. In return, the core of the dynamics is reduced to a set of ordinary differential equations. Using such a model, one may generate waveform templates, which are according to contemporary consensus necessary for the analysis of data from the LISA instrument. This makes the study of this system very important for future gravitational wave observations.

The simplest approximation for this motion is a point particle moving along a geodesic, neglecting the body's finite size. In the Kerr spacetime background, which is assumed to describe a spinning black hole, the geodesic equations of motion are separable, the system is integrable and one can find no prolonged resonances or chaotic orbits. One degree of approximation finer, the finite size effect caused by the body's rotation (similar to the force an electromagnetic field exerts on a dipole) is included and a point particle evolving with this effect taken into account is called a *spinning particle*. This finite size effect will demonstrate itself in the orbital phase of the waveform at next-to-leading order in the mass ratio, making it an indispensable piece of waveform modeling frameworks [8].

An EMRI model that employs a spinning particle as the stellar mass compact

object is in general non-integrable, displaying chaotic behavior and prolonged resonances. The equations of motion are, however, approximately separable. It is unclear whether this means that chaos doesn't appear at linear order in spin. This needs to be discovered to determine the role resonances play in EMRIs and to make accurate predictions for LISA waveforms.

In this thesis we restrict ourselves to a non-spinning supermassive black hole, described by the Schwarzschild spacetime background, and the corresponding gravitational wave emission. We consider the spinning particle and demonstrate the emergence of chaos using the Poincaré section, rotation number and recurrence analysis. We also make use of a time-domain Teukolsky code to establish a link between dynamical features of the spinning particle system and of the radiated gravitational waveforms.

The organization of the thesis is as follows: in the first chapter, we summarize some basic theoretical results concerning the equations of motion of spinning particles, regular and chaotic behavior and the Schwarzschild spacetime. In the second chapter, we demonstrate how resonances grow with spin, in the third chapter, we compute gravitational waveforms from the studied system, and in the fourth chapter, we use recurrence analysis to establish a link between chaos in the motion and in the waveforms.

List of Abbreviations

AA action-angle

CFL Courant-Friedrichs-Lewy

dof degree of freedom

EMRI Extreme Mass Ratio Inspiral

FNN false nearest neighbor

KAM Kolmogorov-Arnold-Moser

MPD Mathisson-Papapetrou-Dixon

ODE ordinary differential equation

RR recurrence rate

SSC spin supplementary condition

TD Tulczyjew-Dixon

1. Spinning particles in the Schwarzschild spacetime

1.1 Equations of motion for spinning particles

1.1.1 Mathisson-Papapetrou-Dixon equations

We will use Greek indices $\mu, \nu, ... = t, r, \theta, \phi$ to denote coordinate components of tensors and capital latin indices $A, B, ... = 0, 1, 2, 3$ to denote tetrad components. The metric signature convention used is $(-, +, +, +)$. As is usual, a dot above a symbol denotes the absolute derivative with respect to the proper time $\dot{A}^{\mu\cdots}_{\nu\cdots} = \mathrm{D}A^{\mu\cdots}_{\nu\cdots}/\mathrm{d}\tau$ and indices separated by a comma or semicolon denote a partial or covariant derivative, respectively. The sign convention for the Riemann tensor is that $2\omega_{\rho;[\mu\nu]} := \omega_\sigma R^\sigma{}_{\rho\mu\nu}$ for any covector field ω.

We attempt to model an Extreme Mass Ratio Inspiral as the motion of an extended body in the fixed spacetime background of a static black hole. This motion can be described by a comprehensive multipole formalism developed by Dixon [9, 10, 11]. The worldline of a particle $x^\mu(\tau)$ is parameterized by the proper time defined by

$$\mathrm{d}\tau^2 := -g_{\mu\nu}\mathrm{d}x^\mu \mathrm{d}x^\nu \,. \tag{1.1}$$

If one concerns oneself with only the gravitational interaction and restricts the multipole expansion of the extended body to the monopole and dipole terms by neglecting the quadrupole and higher-order moments, the equations of motion reduce to the Mathisson-Papapetrou-Dixon (MPD) equations (see [12, 13]). Neglecting the dipole term in the expansion as well would yield geodesic motion.

The MPD equations read

$$\dot{P}^\mu = -\frac{1}{2}R^\mu{}_{\nu\rho\sigma}u^\nu S^{\rho\sigma} \,, \tag{1.2a}$$

$$\dot{S}^{\mu\nu} = 2P^{[\mu}u^{\nu]} = P^\mu u^\nu - P^\nu u^\mu \,, \tag{1.2b}$$

where $S^{\mu\nu}$ is the spin-tensor, P^μ is the four-momentum and $u^\mu = \mathrm{d}x^\mu/\mathrm{d}\tau$ is the four-velocity. If we define the kinematical mass

$$m := -P_\mu u^\mu \tag{1.3}$$

and the dynamical mass

$$\mu := \sqrt{-P_\mu P^\mu} \,, \tag{1.4}$$

then

$$P^\mu = mu^\mu - u_\sigma \dot{S}^{\mu\sigma} \,. \tag{1.5}$$

Another useful quantity is the spin magnitude

$$S := \sqrt{\frac{1}{2}S_{\mu\nu}S^{\mu\nu}} \,. \tag{1.6}$$

For a continuous symmetry of the spacetime background with the corresponding Killing vector field ξ, this system admits an integral of motion in the form [14]

$$C(\xi) = P_\sigma \xi^\sigma - \frac{1}{2}\xi_{\rho;\sigma}S^{\rho\sigma} \,. \tag{1.7}$$

1.1.2 Spin supplementary condition

The MPD equations do not fully determine the system's evolution. Therefore, it is necessary to specify an additional spin supplementary condition (SSC). It takes on the form

$$V_\mu S^{\mu\nu} := 0 \,, \tag{1.8}$$

where V is a time-like vector. The meaning of an SSC is related to the multipole formalism [9]: one describes the extended body using its multipole moments, the V in Eq. (1.8) determines the frame used to calculate these moments. Several different SSCs have been proposed (see, e.g., [8, 15]); however, the existence of a four-vector V such that Eq. (1.8) holds is already a constraint on the system: in geometrical terms, one may write any 2-form as

$$S = \alpha \wedge \beta + \gamma \wedge \delta \,, \tag{1.9}$$

where α through δ are covectors; if there were more terms, the respective covectors would be linearly dependent for any S and it could be again reduced to the form above. If this were indeed the simplest possible form for the spin-tensor, α through δ would form a basis of the cotangent space and $V \cdot S$ would be a linear combination of the elements of this basis, which can never be zero. Thus, the spin-tensor may be written as $S = \alpha \wedge \beta$, this leads to $\epsilon_{\mu\nu\rho\sigma} S^{\mu\nu} S^{\rho\sigma} = 0$.

In this thesis we use the Tulczyjew-Dixon (TD) SSC

$$P_\mu S^{\mu\nu} = 0 \,. \tag{1.10}$$

Due to this condition, the dynamical mass and the spin magnitude are integrals of motion. The system as given above together with the SSC leads to the equation [8]

$$u^\mu := \frac{\mathrm{d}x^\mu}{\mathrm{d}\tau} = \frac{m}{\mu^2}\left(P^\mu + \frac{2 S^{\mu\nu} R_{\nu\gamma\kappa\lambda} P^\gamma S^{\kappa\lambda}}{4\mu^2 + R_{\chi\eta\omega\xi} S^{\chi\eta} S^{\omega\xi}}\right) \,. \tag{1.11}$$

The kinematical mass can be expressed as

$$m = \frac{\mathcal{A}\mu^2}{\sqrt{\mathcal{A}^2\mu^2 - \mathcal{B}S^2}} \,, \tag{1.12}$$

where

$$\mathcal{A} = 4\mu^2 + R_{\alpha\beta\gamma\delta} S^{\alpha\beta} S^{\gamma\delta} \,, \tag{1.13a}$$

$$\mathcal{B} = 4 h^{\kappa\eta} R_{\kappa\iota\lambda\mu} P^\iota S^{\lambda\mu} R_{\eta\nu\omega\pi} P^\nu S^{\omega\pi} \,, \tag{1.13b}$$

$$h^\kappa{}_\eta = \frac{1}{S^2} S^{\kappa\rho} S_{\eta\rho} \,. \tag{1.13c}$$

Thus, the derivatives $\dot{x}^\mu$, $\dot{P}^\mu$ and $\dot{S}^{\mu\nu}$ are uniquely expressed and the system of ODEs is complete.

1.1.3 Canonical formalism

While the system as discussed so far is a well-defined dynamical system, it is simply a set of ODEs, whereas the symplectic structure of a Hamiltonian system would provide us with tools to identify uninteresting degrees of freedom and

eliminate them from the ODE system. By reducing the degrees of freedom we can easier study dynamical features of the system. We will use the formalism described by Witzany [8]. We only provide a very concise summary; for more detailed information, see the original paper.

We take an orthonormal tetrad $e^{A\mu}$, $g_{\mu\nu}e^{A\mu}e^{B\nu} = \eta^{AB}$ and define the "dual" tetrad as $e^{A}{}_{\mu} := g_{\mu\nu}e^{A\nu}$. The new phase space coordinates are defined by

$$x^{\mu}\,, \tag{1.14a}$$

$$p_{\mu} := P_{\mu} + \frac{1}{2}e_{A\nu;\mu}e_{B}{}^{\nu}S^{AB}\,, \tag{1.14b}$$

$$S^{AB} := e^{A}{}_{\mu}e^{B}{}_{\nu}S^{\mu\nu}\,. \tag{1.14c}$$

With the Poisson brackets

$$\{x^{\mu}, p_{\nu}\} = \delta^{\mu}_{\nu}\,, \tag{1.15a}$$

$$\{S^{AB}, S^{CD}\} = \eta^{AC}S^{BD} - \eta^{AD}S^{BC} + \eta^{BD}S^{AC} - \eta^{BC}S^{AD}\,, \tag{1.15b}$$

$$\{x^{\mu}, x^{\nu}\} = \{p_{\mu}, p_{\nu}\} = \{x^{\mu}, S^{AB}\} = \{p_{\mu}, S^{AB}\} = 0\,, \tag{1.15c}$$

the Hamiltonian

$$H = \frac{m}{2\mu^2}\left[\left(g^{\mu\nu} - \frac{4S^{\nu\gamma}R^{\mu}{}_{\gamma\kappa\lambda}S^{\kappa\lambda}}{4\mu^2 + R_{\chi\eta\omega\xi}S^{\chi\eta}S^{\omega\xi}}\right)P_{\mu}P_{\nu} + \mu^2\right]\,. \tag{1.16}$$

generates the system of MPD equations with the TD SSC. There is a further transformation to obtain canonical variables; again, the interested reader is referred to [8]. For the purposes of this work, its existence is enough. Adding the spin with the TD SSC to the geodesic system leads to only one additional degree of freedom (dof) [8].

1.2 Dynamical systems

This section summarizes the most elementary findings about non-linear dynamical systems. For a more comprehensive insight into the topic, see [16, 17, 18].

1.2.1 Integrable systems

An important notion is that of an integrable system, which is closely connected to integrals of motion. Let us consider an autonomous Hamiltonian system with N degrees of freedom (dof's), i.e. a $2N$-dimensional phase space, with canonical coordinates $q^i, p_i, i = 1, 2, \ldots, N$ and Hamiltonian H. Let us also assume that there exists a non-trivial integral of motion $I : \{I, H\} = 0$. This way, not only is the motion restricted to a $2N-1$-dimensional subset of the phase space, but due to the symplectic structure, this allows for a separation of a full dof, as there exists a canonical transformation to variables wherein one of the canonical momenta is the integral I, e.g., $p_1 = I$, and thus the Hamiltonian does not depend on the corresponding position, i.e. q^1. This way, the evolution of $q^i, p_i, i \neq 1$ is not influenced by the first dof and by setting a value for the integral I, it is possible to study the system only concerning the variables $q^i, p_i, i \neq 1$ and I becomes a

parameter of the system $q^i, p_i, i \neq 1$. We call this the *reduced system* and say that it evolves on a submanifold of the original phase space.

In the case of $n > 1$ integrals of motion $I_i, i = 1, 2, \ldots, n$, one can reduce the phase space by n dof under additional conditions. If the integrals are linearly independent ($\det(I_{i,j}) \neq 0$) and in involution ($\{I_i, I_j\} = 0\,, \forall\ i, j$), a canonical transformation exists which equates several momenta with the integrals, e.g. $p_i = I_i, i = 1, 2, \ldots, n$, and the Hamiltonian is independent of the corresponding positions, i.e. $q^i, i = 1, 2, \ldots, n$. Then the evolution of variables $q^i, p_i, i = n+1, \ldots, N$ is independent of the separated dof and we call it the reduced system. All the separated dof are also independent of each other.

If one assumes the existence of N independent integrals of motion in involution, one of which is the Hamiltonian, then one can separate all the dof's and they all become independent, simplifying the motion greatly. This is expressed by the Liouville theorem, which states that there exists a set of variables θ^i, I_i such that:

$$\theta^i(\tau) = \theta^i(0) + \tau\omega^i(I_j)\ , \tag{1.17a}$$

$$I_i(\tau) = I_i(0)\ . \tag{1.17b}$$

The system is then called *integrable* and all of the coordinates evolve by a linear evolution law. In addition, if the motion is bounded, then it lies on a nested family of N-dimensional tori (see, e.g., [16]). The θ^i variables are then typically 2π-periodic and the ω^i's are the characteristic frequencies.

As we will see later, the relevant system in this work possesses enough integrals to be reduced to two degrees of freedom, so from now on, we will restrict ourselves to systems with $N = 2$ and bounded motion.

In an integrable system, the ratio of characteristic frequencies is known as the *rotation number* $\omega = \omega^1/\omega^2$. When $\omega \in \mathbb{Q}$, the motion is periodic, as there exists a time after which both $\tau\omega^i$'s are integer multiples of 2π; the torus is called *resonant* and the corresponding phase space region is called a *resonance*. On the other hand, if $\omega \in \mathbb{R} \setminus \mathbb{Q}$, the orbit densely covers the whole torus (this is called quasiperiodic motion).

A very powerful phase space visualization tool is the *Poincaré section*. Orbits lie on a hypersurface of constant Hamiltonian in the phase space. In it, one can choose a 2-dimensional surface $\mathcal{S}$, which is transversal to the Hamiltonian flow, i.e., nowhere on $\mathcal{S}$ does the Hamiltonian flow lie in the tangent plane to $\mathcal{S}$. We call such a hypersurface the *surface of section* or Poincaré section. By considering succesive intersections of a trajectory with $\mathcal{S}$, the original 2-dof continuous-time system is converted to a 1-dof discrete-time system. We call the mapping of one intersection with $\mathcal{S}$ to another the *return mapping* and denote it as $\Omega : \vec{x}_{n+1} = \Omega\vec{x}_n$. The return mapping retains symplecticity: it preserves the symplectic form, the tensor which generates the Poisson bracket [17].

In the case of an integrable system, all intersections corresponding to a single non-resonant trajectory will lie on the intersection of an invariant torus and $\mathcal{S}$, which will appear as a closed curve (usually called an invariant circle). For a resonant torus with $\omega = r/s$, the intersection will be an invariant circle as well; a single trajectory, on the other hand, will only form a finite set of s periodic points in the surface of section. These are often called fixed points, as they are preserved

by Ω^s. This method is widely used for studying non-linear systems which can be reduced to 2 dof's (see, e.g., [19, 20]).

We define another key property: a map is said to be a *twist map*, if there is a center such that the map rotates points with respect to the center by an angle which changes monotonically with the distance from the center. The return mapping in a Hamiltonian system quite often has this property [17], but it is not always true. Consequently, if the Poincaré section defined by $\theta^2 = 0 \mod 2\pi$ is a twist map, then the rotation number changes monotonically in the direction to the outermost circles. In this case, there is also a practical method to evaluate the rotation number. One must identify the period-1 fixed point $\vec{x}_c$ in the surface of section and take angles between successive intersections $\vec{x}_i$ with the surface of section with respect to $\vec{x}_c$ as

$$\vartheta_i := \operatorname{ang}\left[\left(\vec{x}_{i+1} - \vec{x}_c\right), \left(\vec{x}_i - \vec{x}_c\right)\right] . \tag{1.18}$$

Then the rotation number, up to an additive integer, can be determined as

$$\nu_\vartheta := \lim_{n\to\infty} \frac{1}{2\pi n} \sum_{i=1}^{n} \vartheta_i . \tag{1.19}$$

If the trajectory lies on an invariant torus, then $\nu_\vartheta = \omega \mod 1$ [21]. The error of the limit for finite n is bounded by $1/n$. Intuitively, $2\pi\nu_\vartheta$ is the average angle by which the return mapping rotates a point of the given trajectory in the surface of section with respect to the central period-1 fixed point.

1.2.2 Perturbation

The structure as described in the previous subsection fully applies only in the integrable case. Upon application of a small perturbation, one typically gets what is called a near-integrable system, which is not integrable anymore, but it retains a lot of structure from the integrable system.

As described in the previous subsection, the surface of section of an integrable system is formed by a family of nested invariant circles, with the rotation number monotonically changing outwards. While the application of a small perturbation breaks integrability, many of these circles remain in the perturbed system as well. The ones which survive sufficiently small perturbations are those "far enough from resonances"; this is formally expressed through the notion of Diophantine numbers. We say that a number $\omega \in \mathbb{R}$ is q-Diophantine ($q \geq 1$) if

$$\exists C > 0 : \forall (m, n) \in \mathbb{Z}^2 \setminus \{(0, 0)\} : |n\omega - m| > \frac{C}{n^q} \tag{1.20}$$

and the property expresses that ω cannot be well approximated by rational numbers. The Kolmogorov-Arnold-Moser (KAM) theorem states that for j-times differentiable mapping and perturbation, there are invariant circles with q-Diophantine rotation numbers for $q \in (1, (j-1)/2)$, if the perturbation is sufficiently small [17]. The set bounded by the outermost invariant circle is then called the *main island of stability*.

The KAM theorem does not say anything about what happens to resonances after the perturbation. The Poincaré-Birkhoff theorem [16] states that for the

resonance $\omega = r/s$ in the integrable system, $2ns$ of the periodic points remain even in the perturbed system, where $n \in \mathbb{N}$. Properties of these periodic points can be studied using the notion of linear stability, that is, linearizing the mapping around the periodic point and studying the matrix of the linearized map and its eigenvalues λ_1 and λ_2. Because the map is real, it must hold $\bar{\lambda}_1 = \lambda_2$ and from symplecticity it follows that $\lambda_1 \cdot \lambda_2 = 1$, so there exist three distinct behaviors:

- $\lambda_1, \lambda_2 \in \mathbb{C} \setminus \mathbb{R}$: from the conditions above, both eigenvalues lie on the unit circle. In the vicinity of the point the linearized mapping moves on an ellipse and an *island of stability* arises. This kind of fixed point is called stable or elliptic,
- $\lambda_1, \lambda_2 \in \mathbb{R}$: this results in linearized motion on a hyperbola. This kind of fixed point is called unstable or hyperbolic,
- $\lambda_1 = \lambda_2 = \pm 1$: this point is called indifferently stable.

As stated in the Poincaré-Birkhoff theorem, after the perturbation half of the surviving periodic points in a given resonance are elliptic and the other half hyperbolic.

To see what happens near a hyperbolic fixed point $\vec{x}_f$, we make use of invariant manifolds. We define:

$$W^s(\vec{x}_f) := \{\vec{x} \in \mathcal{S} : \Omega^n \vec{x} \overset{n\to\infty}{\longrightarrow} \vec{x}_f\} , \tag{1.21a}$$

$$W^u(\vec{x}_f) := \{\vec{x} \in \mathcal{S} : \Omega^n \vec{x} \overset{n\to-\infty}{\longrightarrow} \vec{x}_f\} . \tag{1.21b}$$

Due to the stable manifold theorem [22], these sets fulfill the definition of a manifold and we call them the *stable* and *unstable manifold*, respectively; these manifolds cannot intersect themselves. They are called invariant, since

$$\Omega W^s(\vec{x}_f) = W^s(\vec{x}_f) , \quad \Omega W^u(\vec{x}_f) = W^u(\vec{x}_f) . \tag{1.22}$$

In addition, the Hartman-Grobman theorem [23] states that the return mapping is topologically equivalent to the linearized mapping near an unstable fixed point.

By definition, for two fixed points $\vec{x}_{f1} \neq \vec{x}_{f2}$:

$$W^s(\vec{x}_{f1}) \bigcap W^s(\vec{x}_{f2}) = \varnothing , \tag{1.23a}$$

$$W^u(\vec{x}_{f1}) \bigcap W^u(\vec{x}_{f2}) = \varnothing . \tag{1.23b}$$

However, intersections of $W^s(\vec{x}_{f1})$ and $W^u(\vec{x}_{f2})$ can exist. They are called *heteroclinic points* if $\vec{x}_{f1} \neq \vec{x}_{f2}$ and *homoclinic points* if $\vec{x}_{f1} = \vec{x}_{f2}$. From their definition it follows that if one homoclinic point exists (except for the fixed point itself), countable infinite such points exist and form a *homoclinic orbit*, which has a different topology than a KAM curve. The same argument applies for a heteroclinic point and corresponding heteroclinic orbit; the invariant manifolds with homoclinic and heteroclinic points are shown in Fig. 1.1. Homoclinic orbits in a resonance generically exist and form the basis for *homoclinic chaos*, when many intersections of an orbit starting near the unstable point densely fill a two-dimensional subset of $\mathcal{S}$.

If one focuses at a secondary island in the r/s resonance and studies the behavior of Ω^s, all of the previous arguments hold as well, leading to a self-similar

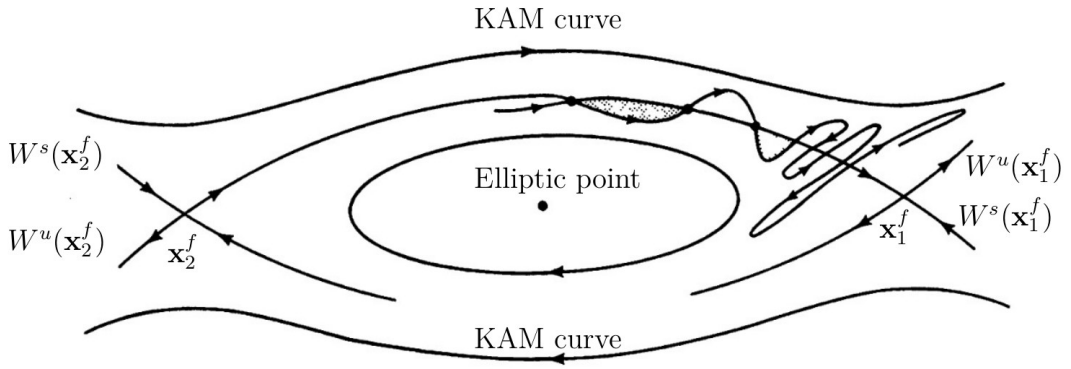

Figure 1.1: Typical example of the resonant structure in near-integrable systems. Figure taken from [16].

structure of the resonance, displaying all the same features such as secondary resonances and islands of stability with their corresponding hyperbolic points. In this region, many of both homoclinic and heteroclinic orbits generically exist, forming the very complicated dynamics in the resonance and being the drivers of so-called *heteroclinic chaos*.

This finally leads us to a complete picture of the perturbed phase space: there remains a central fixed point with many quasi-periodic KAM circles, forming the main island of stability. In the resonances arise chaotic regions, densely filled by a single orbit, and islands of stability. These are remarkably similar to the main island of stability, leading to tertiary islands of stability etc. At every order, one can find higher-order resonances, elliptic points with islands of stability and hyperbolic points with heteroclinic and homoclinic orbits. This type of structure is depicted in Fig. 1.2.

The quantity ν_ϑ defined in the previous section can also be helpful to visualize the phase space of a near-integrable system. If one chooses a parametrized line of initial conditions in the surface of section, computes the ν_ϑ for each of them and plots it as a function of the initial condition, one obtains the *rotation curve*. If the initial conditions are chosen so that they only cross invariant circles in one direction, then the rotation curve of an integrable system is monotonous. Since the near-integrable system retains most of the invariant circles from the unperturbed case, the corresponding rotation curve mostly fulfills this as well, except when passing through a resonance. Initial conditions in the same island of stability lead to the same ν_ϑ, forming a plateau in the rotation curve. Multiple initial conditions in a chaotic region, however, lead to unpredictable values and wildly differ. Thus, one can detect resonances in a near-integrable system by either a plateau or non-monotonous variations in the rotation curve.

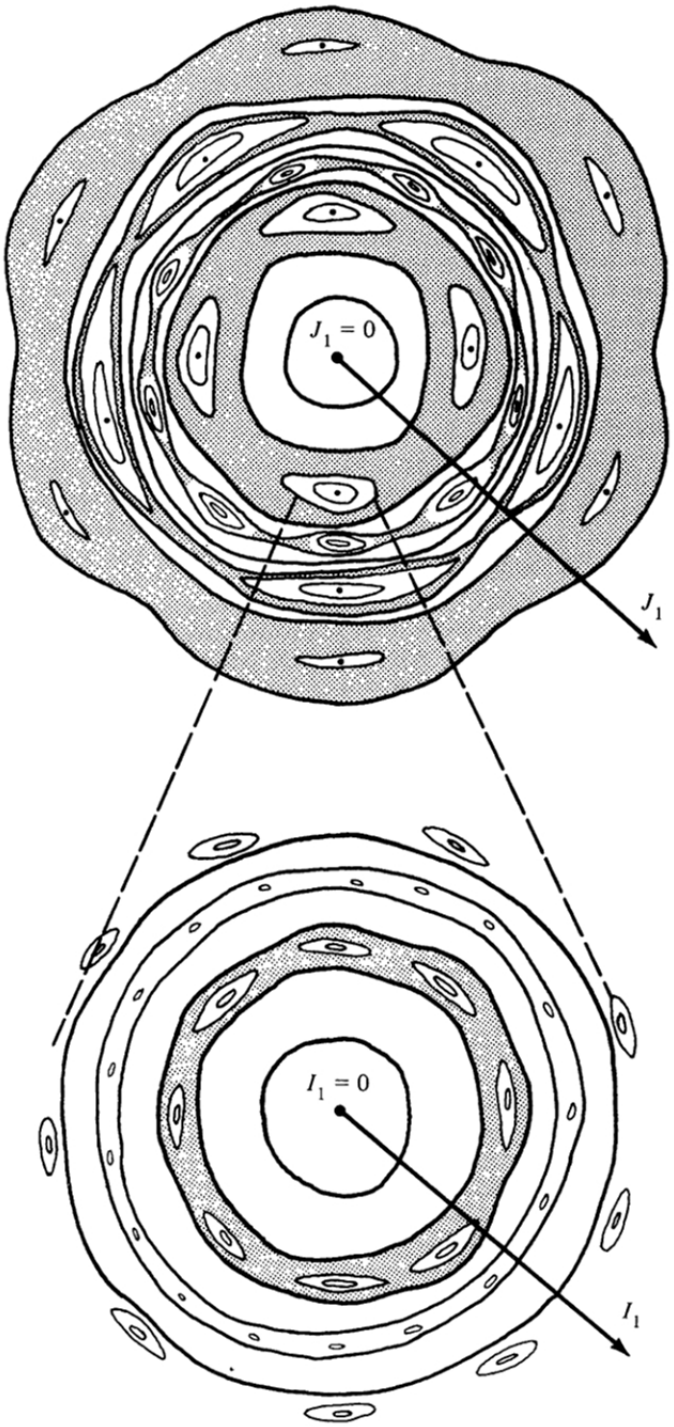

Figure 1.2: A schematic picture of a near-integrable system. Top part: in the middle there is the period-1 fixed point, the center of the main island of stability; there are KAM circles around it with resonances between them, consisting of smaller islands of stability and the homoclinic chaotic region. Bottom part: a close-up of a secondary island of stability, revealing the self-similar structure, showing tertiary islands of stability and related features. The figure is taken from [16].

1.3 In the Schwarzschild spacetime

1.3.1 Schwarzschild spacetime

The Schwarzschild metric, describing a non-spinning black hole of mass M, is in Schwarzschild coordinates given by the line element

$$g_{\mu\nu}\mathrm{d}x^{\mu}\mathrm{d}x^{\nu} = -f\left(r\right)\mathrm{d}t^{2} + \frac{1}{f\left(r\right)}\mathrm{d}r^{2} + r^{2}\left(\mathrm{d}\theta^{2} + \sin^{2}\theta\mathrm{d}\phi^{2}\right) , \tag{1.24}$$

where

$$f\left(r\right) = 1 - \frac{2M}{r} . \tag{1.25}$$

The spacetime is stationary and spherically symmetric, i.e. there exist a timelike Killing vector field and three spacelike Killing vector fields which, with the Lie bracket, generate the $\mathfrak{so}(3)$ algebra. They are

$$\xi_{(t)} = \frac{\partial}{\partial t} , \tag{1.26a}$$

$$\xi_{(x)} = -\sin\phi\frac{\partial}{\partial\theta} - \cos\phi\cot\theta\frac{\partial}{\partial\phi} , \tag{1.26b}$$

$$\xi_{(y)} = \cos\phi\frac{\partial}{\partial\theta} - \sin\phi\cot\theta\frac{\partial}{\partial\phi} , \tag{1.26c}$$

$$\xi_{(z)} = \frac{\partial}{\partial\phi} . \tag{1.26d}$$

1.3.2 Integrals of motion

The formula for integrals of motion in Eq. (1.7) can be expressed for computational convenience using either the P_{μ} or the canonical p_{μ} as

$$\begin{aligned} C(\xi) = P_{\sigma}\xi^{\sigma} - \frac{1}{2}g_{\rho\alpha}\xi^{\alpha}{}_{,\sigma}S^{\rho\sigma} - \frac{1}{2}g_{\beta\rho,\sigma}\xi^{\beta}S^{\rho\sigma} = \\ p_{\sigma}\xi^{\sigma} - \frac{1}{2}g_{\rho\alpha}\xi^{\alpha}{}_{,\sigma}S^{\rho\sigma} - \frac{1}{2}g_{\alpha\nu}\xi^{\mu}e_{A}{}^{\alpha}{}_{,\mu}e_{B}{}^{\nu}S^{AB} . \end{aligned} \tag{1.27}$$

Together with the tetrad

$$e_0 = \frac{1}{\sqrt{f}}\frac{\partial}{\partial t} , \quad e_1 = \sqrt{f}\frac{\partial}{\partial r} , \tag{1.28a}$$

$$e_2 = \frac{1}{r}\frac{\partial}{\partial\theta} , \qquad e_3 = \frac{1}{r\sin\theta}\frac{\partial}{\partial\phi} , \tag{1.28b}$$

the Killing fields in Eqs. (1.26) give rise to the integrals

$$E := -C(\xi_{(t)}) = -p_t = -P_t - \frac{M}{r^2} S^{tr} \,, \tag{1.29a}$$

$$\begin{aligned} J_x := \quad C(\xi_{(x)}) &= -\sin\phi\, p_\theta - \cos\phi\, \cot\theta\, p_\phi + r^2 \cos\phi\, S^{\theta\phi} \\ &= -\sin\phi\, P_\theta - \cos\phi\, \cot\theta\, P_\phi + r^2 \cos\phi\, \sin^2\theta\, S^{\theta\phi} \\ &\quad + r\sin\phi\, S^{\theta r} + r\cos\phi\, \sin\theta\, \cos\theta\, S^{\phi r} \,, \end{aligned} \tag{1.29b}$$

$$\begin{aligned} J_y := \quad C(\xi_{(y)}) &= \cos\phi\, p_\theta - \sin\phi\, \cot\theta\, p_\phi + r^2 \sin\phi\, S^{\theta\phi} \\ &= \cos\phi\, P_\theta - \sin\phi\, \cot\theta\, P_\phi + r^2 \sin\phi\, \sin^2\theta\, S^{\theta\phi} \\ &\quad - r\cos\phi\, S^{\theta r} + r\sin\phi\, \sin\theta\, \cos\theta\, S^{\phi r} \,, \end{aligned} \tag{1.29c}$$

$$J_z := \quad C(\xi_{(z)}) = p_\phi = P_\phi - r\sin^2\theta\, S^{\phi r} - r^2 \sin\theta\, \cos\theta\, S^{\phi\theta} \,. \tag{1.29d}$$

Using these, we define the measure of the total angular momentum as

$$J^2 = J_x^2 + J_y^2 + J_z^2 \,, \tag{1.30}$$

and by taking the Poisson bracket (1.15) we can see that

$$\{E, J_j\} = 0 \,, \tag{1.31a}$$

$$\{J_i, J_j\} = -\epsilon_{ijk} J_k \,, \tag{1.31b}$$

$$\{J^2, J_j\} = 0 \,. \tag{1.31c}$$

The two previously mentioned integrals (spin magnitude $S^2 = \sqrt{S_{\mu\nu} S^{\mu\nu}/2}$ and the expression $\epsilon_{\mu\nu\rho\sigma} S^{\mu\nu} S^{\rho\sigma} = 0$) are preserved as well; however, in the construction of the canonical formalism, the earlier is a parameter of the transformation and the latter is assumed as well.

1.3.3 Reduction of system

The system as described so far has 4 spacetime degrees of freedom and 1 spin degree of freedom [8]. It is possible to use integrals of motion - in this case, E, J_z and J^2 - to reduce the dof to only 2, as described in detail in Subsec. 1.2.1. We have seen in Eq. (1.31) that they truly are in involution. This amounts to picking specific values of E, J_z and J^2, which then become parameters of the reduced system.

In fact, we can go further: due to spherical symmetry of the Schwarzschild spacetime, for every orbit there exists a coordinate system such that the total angular momentum is aligned with the z-axis ($\theta = 0$) [24]. Thus, every relevant feature of the system's dynamics remains covered by making the choice

$$J_x = J_y = 0 \,. \tag{1.32}$$

Due to this, we can write

$$\begin{pmatrix} 0 \\ 0 \end{pmatrix} = \begin{pmatrix} J_x \\ J_y \end{pmatrix} = \begin{pmatrix} \cos\phi & -\sin\phi \\ \sin\phi & \cos\phi \end{pmatrix} \begin{pmatrix} -\cot\theta\, p_\phi + r^2 S^{\theta\phi} \\ p_\theta \end{pmatrix} \,, \tag{1.33}$$

and thus

$$p_\theta = -\cot\theta\, p_\phi + r^2 S^{\theta\phi} = 0 \,. \tag{1.34}$$

A useful tool to get an elementary insight into the motion is an effective potential. We use the effective potential taken from [24], which gives the energy of a particle with $P_r = P_\theta = 0$ and the given J_z and S in the point r, θ. It has two branches and reads

$$V_{\text{eff}\,(\pm)} = \mu \left[\sqrt{f} \cosh X_{(\pm)} + \frac{M \sinh X_{(\pm)}}{\sqrt{f} r \cosh X_{(\pm)}} \cdot \left(\frac{J \sin\theta}{\mu r} - \sinh X_{(\pm)} \right) \right] , \tag{1.35a}$$

$$\sinh X_{(\pm)} = \frac{\mu J r \sin\theta}{\mathcal{D}} \pm \frac{1}{\mathcal{D}} \sqrt{(\mu J r \sin\theta)^2 - \left[(J^2 - S^2) f + \frac{2M}{r} J^2 \sin^2\theta \right] \mathcal{D}} , \tag{1.35b}$$

$$\mathcal{D} = \mu^2 r^2 - S^2 f . \tag{1.35c}$$

In the limit $r \to \infty$, non-negativity of the square root argument leads to the requirement

$$\cos\theta \leq \frac{S}{J} , \tag{1.36}$$

and for finite r, it seems to be even slightly more restrictive. This means that for low spin values the particle can only move in a thin disk near the equatorial plane. In the limiting geodesic case $S \to 0$, the particle is confined to the equatorial plane (recall that we have imposed the constraint $J^2 = J_z^2$!).

For high values of the spin, we cannot make general statements about the effective potential; however, for $S \ll \mu M$, it will only deviate slightly from its geodesic counterpart. The typical shapes of $V_{\text{eff}(\pm)}$ are shown in Fig. 1.3, where we can see the band of r and E values allowed as initial conditions when considering $P_r = 0$ with the geodesic effective potential running between them and the corresponding Poincaré section. One can see that in the outer part of the surface of section still within the band of admissible initial conditions, there are no points: the corresponding initial conditions exist but correspond to fast plunging orbits most of which only intersect the surface of section very few times before plunging into the central object and therefore do not form structures in the figure.

1.4 Initial conditions

In this section, we describe the choice of initial conditions for numerical integration of orbits. To gain insight into the phase space dynamics, we reduce the system to only 2 degrees of freedom as described in the previous section. In particular, for every orbit, we will choose the values of the energy E, total angular momentum $J = \sqrt{J^2}$ and spin $S = \sqrt{S^2}$.

Since the motivation for this work are EMRIs, it is necessary to pick values of the spin which are astrophysically relevant. The extended body we are modeling can be either a

- stellar mass black hole, in which case calculations with the Kerr spacetime show that $S \leq \mu^2$, or
- neutron star, wherein due to the mass shedding limit $S \lesssim 0.6\mu^2$ (see, e.g., [25]).

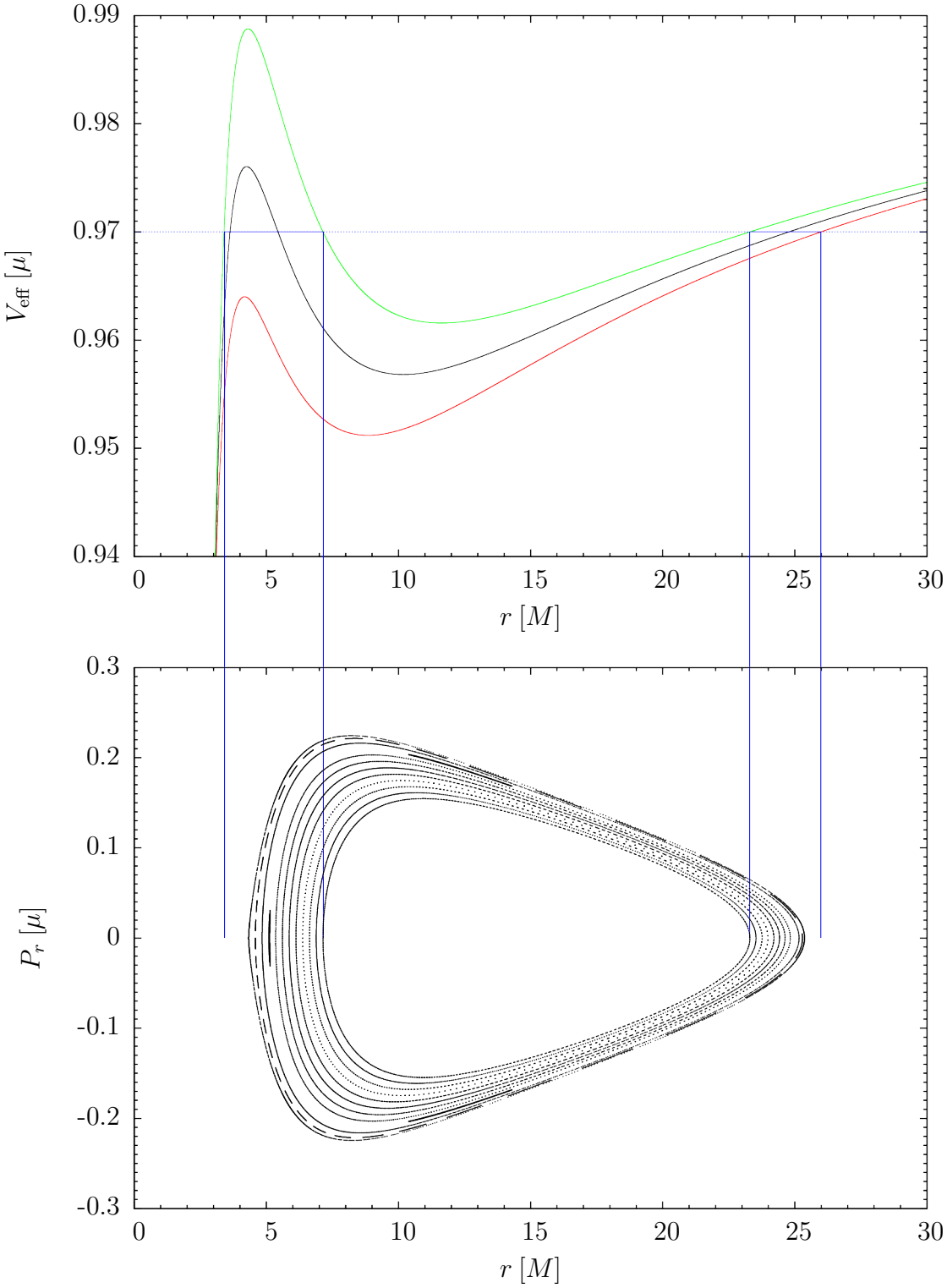

Figure 1.3: Top panel: The effective potential in the equatorial plane for $J_z = 3.8\mu M$. The black line corresponds to $S = 0$, red and green lines are $V_{\text{eff}(-)}$ and $V_{\text{eff}(+)}$, respectively, for $S = 0.2\mu M$. The blue dotted line shows the energy value $E = 0.97\mu$, the blue full lines show possible initial r with $\theta = \pi/2$ and $P_r = 0$. Bottom panel: The corresponding Poincaré section with 12 initial conditions from $r = 4.327M$ with spacing $0.256M$. The vertical lines connecting both plots show bounds for possible initial r with $P_r = 0$ in the Poincaré section.

The spin in MPD equations in the Schwarzschild spacetime scales as μM and in either case must be bounded by μ^2, thus astrophysically relevant values are

$$S \leq \mu^2 = \frac{\mu}{M} \cdot \mu M \lesssim 10^{-4} \cdot \mu M \,, \tag{1.37}$$

where the 10^{-4} is an approximate maximal mass ratio of an EMRI.

As a surface of section $\mathcal{S}$, we choose the equatorial plane $\theta = \pi/2$ with the momentum pointing "down", i.e. $P_\theta \geq 0$. As coordinates on $\mathcal{S}$, we choose the radial coordinate and momentum r, P_r. This is a very usual choice in black hole spacetimes, employed in previous works (see, e.g., [19, 26] and references therein).

Fig. 1.4 shows the left tip of a Poincaré section and corresponding rotation curve for spin value $S = 10^{-4}\ \mu M$. Visible are all the typical features of a near-integrable system: KAM curves in the right, small islands of stability as remnants of resonant tori and dispersed points corresponding to chaotic orbits. Therefore, the MPD equations with the TD SSC exhibit very typical signs of a chaotic system even for a small enough spin value to correspond to an EMRI with $\mu/M \doteq 10^{-4}$.

In Fig. 1.5 we show the Poincaré section for spin $S = 1.4\mu M$, which is much too high to be relevant for an EMRI. It does, however, show the typical behavior of a highly perturbed system: we see a fairly small remnant of the main island of stability and a very large chaotic region. Both figures were computed numerically using the method described in Attachment A.2.

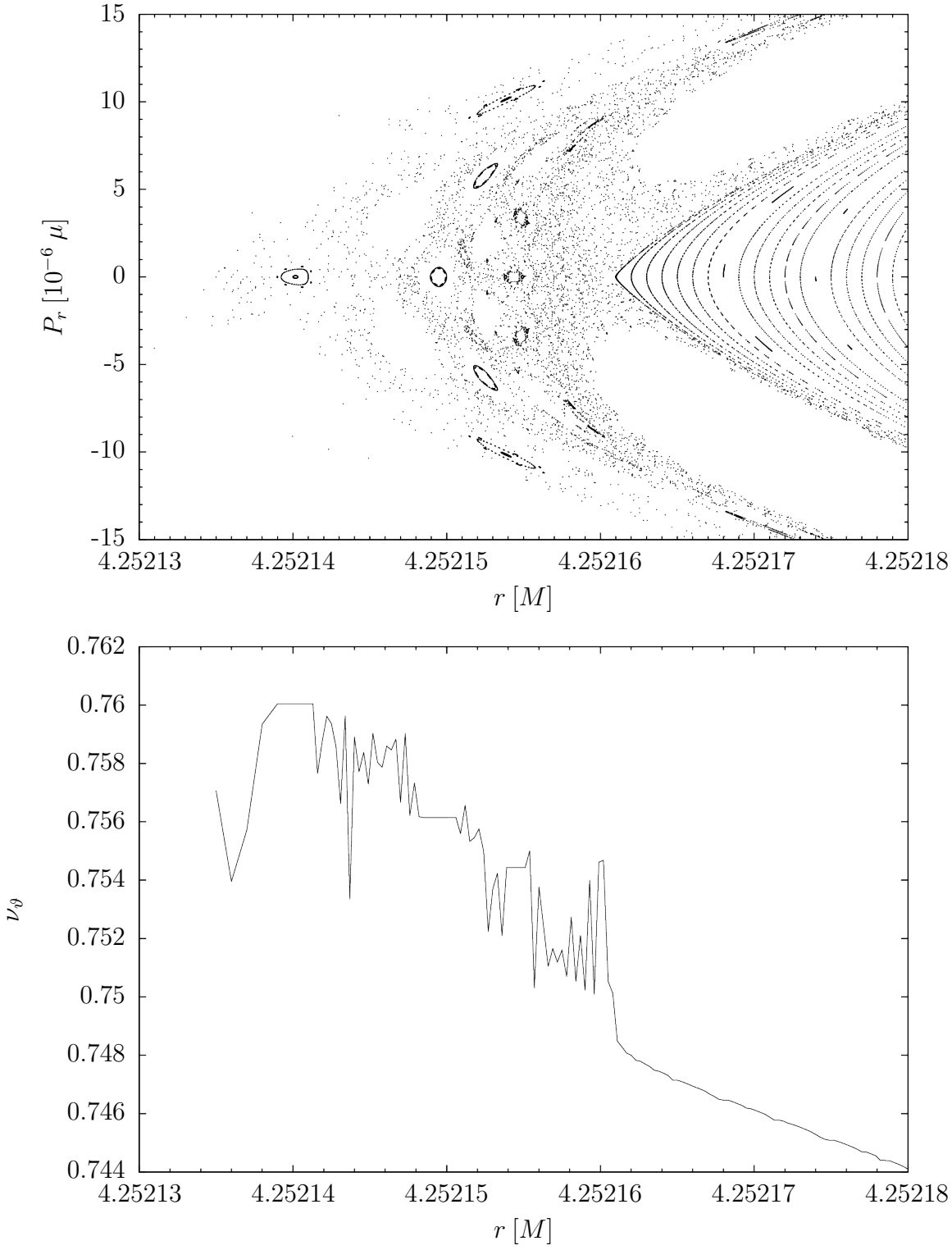

Figure 1.4: Top panel: Poincaré section of the MPD equations for $S = 10^{-4}\,\mu M$, $E = 0.976\mu$, $J_z = 3.8\mu M$ and initial $P_r = 0$. Initial r are 31 equidistant values from $4.252135M$ with the spacing $10^{-6}\ M$. Bottom panel: rotation curve corresponding to the top panel.

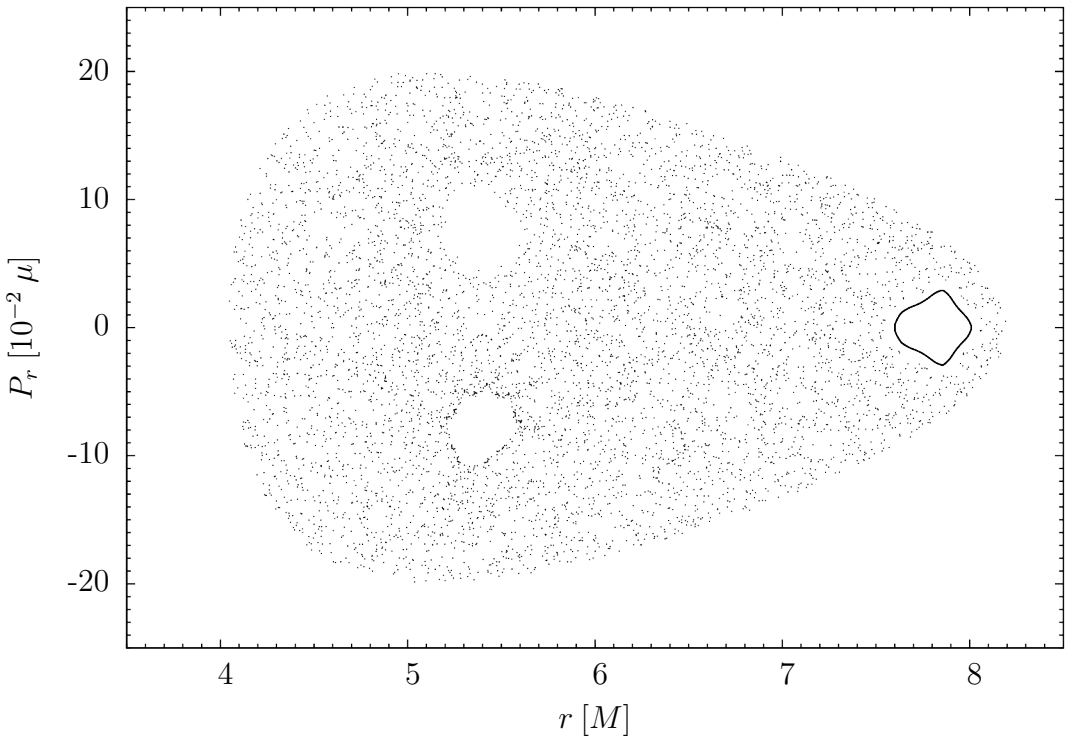

Figure 1.5: A Poincaré section of the MPD equations for $S = 1.4\mu M$, $E = 0.922\,929\,41\mu$, $J_z = 4.0\mu M$ and initial $P_r = 0$ shows a regular orbit with initial $r = 7.6M$ and a chaotic orbit with initial $r = 4.5M$.

2. Action-angle(-like) variables

2.1 Action-angle variables

As mentioned in the previous chapter, in an integrable system, there exist canonical coordinates in the form of Eq. (1.17). Their existence is connected to the separability of the Hamilton-Jacobi equation into a set of independent ordinary differential equations by assuming the action

$$\mathcal{W} = \sum_{i=1}^{N} \mathcal{W}_i \left(q^i\right) \,. \tag{2.1}$$

If the Hamilton-Jacobi equation is separable in the given variables, the actions are defined as

$$I_i = \oint \frac{\mathrm{d}\mathcal{W}_i}{\mathrm{d}q^i} \mathrm{d}q^i \,, \tag{2.2}$$

where the integral is taken over one loop of the corresponding variable. The angles are then such variables that they fulfill the canonical Poisson bracket

$$\{\theta^i, I_j\} = \delta^i_j \tag{2.3}$$

and are 2π-periodic. The I_i are integrals of motion, i.e.

$$\frac{\partial H}{\partial \theta^i} = 0 \,. \tag{2.4}$$

The values of the actions determine on which phase space torus the motion lies and the angles determine the position on the given torus. This set of coordinates is then called the action-angle (AA) variables.

2.2 Growth of resonances

In a near-integrable system, AA variables cannot be defined for the whole system. Nevertheless, if one defines a set of variables which smoothly reduce to AA variables for no perturbation, it is possible to study the effect of gradual deviation from the integrable case using perturbation theory and series expansions. We have written this section along the lines of [18], for more reference, we also recommend [16], [27].

We assume an integrable Hamiltonian system with 2 degrees of freedom in action-angle variables $\theta^i, I_i, i = 1, 2$ with Hamiltonian $H = H_0\left(I_1, I_2\right)$. To focus on the resonance with rotation number $\omega = r/s$, we define the angle $\varphi^1 := s\theta^1 - r\theta^2$, which, in the integrable case, would be zero. To describe the deviation from the unperturbed system, the Hamiltonian to first order in the perturbation parameter ε can then be written as [18]

$$H = H_0\left(I_1, I_2\right) + \varepsilon H_1\left(\varphi^1, I_1, I_2\right). \tag{2.5}$$

Also expanding the actions $I_i = I_i^0 + \Delta I_i$, one gets to second order in ΔI_1

$$H = \frac{\beta}{2}\left(\Delta I_1\right)^2 + \varepsilon F\left(\varphi^1\right) \,, \tag{2.6}$$

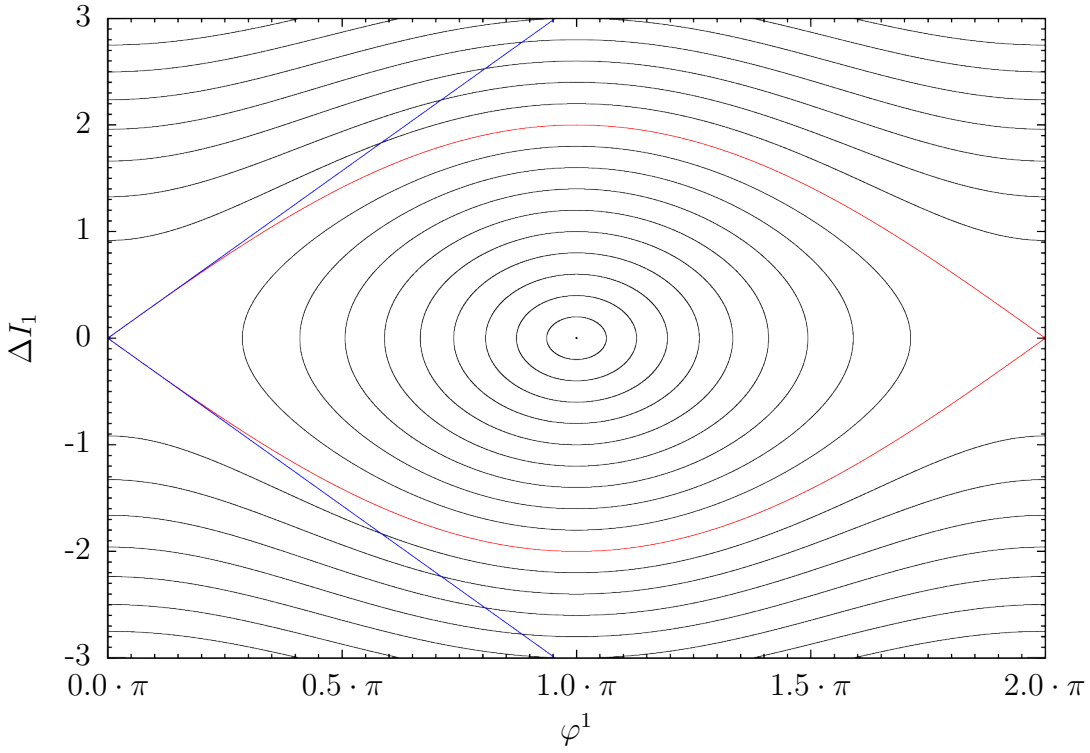

Figure 2.1: Phase portrait of the non-linear oscillator of Eq. (2.7) for $n = 1$ and $\beta = \varepsilon\alpha = 1$. The curve in red is the separatrix, the angle at which it opens is measured between the blue lines and the black lines correspond to trajectories of the system; the ones enclosed between the two separatrix branches correspond to oscillation and the outer ones to libration.

where we have omitted the I_i^0 dependence and the constant term. The last step is to expand the F in a Fourier series and only keep the main term, arriving, without loss of generality, at

$$H = \frac{\beta}{2}\left(\Delta I_1\right)^2 + \varepsilon\alpha\cos\left(n\varphi^1\right) \ . \tag{2.7}$$

For $n = 1$, this is the Hamiltonian of a pendulum, revealing a certain universality of resonances. The separatrix is the curve of constant Hamiltonian, separating the phase space regions corresponding to oscillation and libration: $\varepsilon\alpha = \beta\left(\Delta I_1\right)^2/2 + \varepsilon\alpha\cos\left(n\varphi^1\right)$. The minima of $\cos\left(n\varphi^1\right)$ with $\Delta I_1 = 0$ form stable points and the maxima form unstable points. A straightforward calculation then shows that the resonance has width

$$\text{width} := \max\left(I_1\right) - \min\left(I_1\right) = 4\sqrt{\frac{\varepsilon\alpha}{\beta}} \propto \sqrt{\varepsilon} \ . \tag{2.8}$$

This model also allows us to relate the width to the angle at which the separatrix opens at an unstable point. In a neighborhood of $\varphi^1 = 0$, one may write for the separatrix

$$\Delta I_1 = \pm\sqrt{\frac{\epsilon\alpha}{\beta}} \cdot n\varphi^1 = \pm\frac{\text{width} \cdot n}{4} \cdot \varphi^1 \ . \tag{2.9}$$

Now it is only necessary to return to the original variables $\theta^i, I_i, i = 1, 2$. For a given value of θ^2 - without loss of generality, we can take $\theta^2 = 0$:

$$\theta^1 = \frac{\varphi^1}{s} \ , \tag{2.10}$$

revealing that in the Poincaré section $\theta^2 = 0$, there will be a total of $n \cdot s$ islands in the given resonance. This way we can see that in the weakly perturbed system the n in the discussion above corresponds to the n given in the Poincaré-Birkhoff theorem in Subsec. 1.2.2. This also allows us to finally write the relationship between the resonance width and the local behavior of the separatrix:

$$\Delta I_1 = \pm\frac{\text{width} \cdot ns}{4} \cdot \Delta\theta^1 \ . \tag{2.11}$$

Thus, to determine the width of a resonance in a non-linear system, we can measure the angle at which the separatrix opens - that is, between the Jacobian's eigenvectors at the corresponding unstable periodic point - in AA variables and make use of Eq. (2.11). We can also employ the non-linear oscillator model to estimate the rate at which resonances of a spinning particle near a black hole grow. It has been shown that for MPD equations with the TD SSC to linear order in spin in the Kerr spacetime (of which Schwarzschild is a special case) approximate constants of motion exist that allow for an (approximate) separation of the Hamilton-Jacobi equation (see [28, 29]). It is not clear whether this means that no resonances appear at linear-in-spin order.

As shown above, for a perturbation linear in the parameter ε, resonances grow as width $\propto \sqrt{\varepsilon}$. If the terms linear-in-spin in the equations of motion cause a given resonance to appear, then one can expect the resonance to grow as width $\propto \sqrt{S}$. However, as it is possible that the resonance only appears due to terms which are second order in spin, then we must equate the parameter ε to S^2 and get width $\propto \sqrt{S^2} = S$.

Hence, there are two cases that may appear: width $\propto \sqrt{S}$ or width $\propto S$.

2.3 AA-like variables for the MPD equations

To find a reasonable mapping between our r, P_r surface of section with given E, J_z, $J_x = J_y = 0$, S and a set of AA-like variables, we make use of the geodesic properties: we find a suitable set of fiducial parameters E_f, J_{zf} and use the geodesic $(r, P_r) \leftrightarrow (\theta^r, I_r)$ mapping with these fiducial parameters to convert our Poincaré section data to AA-like variables.

Our approach to finding suitable values for the fiducial parameters relies on the existence of an unstable periodic point $(r_{\mathrm{upo}}, 0)$ near the left tip of the surface of section; our method preserves this unstable point when mapping to the geodesic system. The fiducial parameters are then given by the geodesic formulae

$$E_f = \frac{r_{\mathrm{upo}} - 2M}{\sqrt{r_{\mathrm{upo}}\left(r_{\mathrm{upo}} - 3M\right)}}\mu, \quad J_{zf} = \frac{r_{\mathrm{upo}}}{\sqrt{M\left(r_{\mathrm{upo}} - 3M\right)}}\mu M\,. \tag{2.12}$$

Once the E_f and J_{zf} are known, we propose to convert the point (r, P_r) in the Poincaré section to (θ^r, I_r) as a point on a geodesic with energy E_f, azimuthal angular momentum J_{zf}, radial coordinate r and corresponding momentum P_r passing through the equatorial plane:

$$I_r = I_r^{geo}\left(r; E = E_f, J_z = J_{zf}, \mathcal{C} = r^2\left[\frac{E^2}{f} - f P_r^2 - \mu^2\right] - J_z^2\right)\,, \tag{2.13a}$$

$$\theta^r = \theta_{geo}^r\left(r; E = E_f, J_z = J_{zf}, \mathcal{C} = r^2\left[\frac{E^2}{f} - f P_r^2 - \mu^2\right] - J_z^2\right)\,. \tag{2.13b}$$

As the choice of fiducial parameters E_f, J_{zf} is made using the left tip of the surface of section, the transformation is expected to work well for $r \sim r_{\mathrm{upo}} \Leftrightarrow \theta^r \sim 0$ and might be unsuitable for $r \gg r_{\mathrm{upo}} \Leftrightarrow |\theta^r| \sim \pi$. This is demonstrated in Fig. 2.2, where the previously shown surface of section in Fig. 1.3 is converted to AA-like variables and one can see that for high I_r and low $|\theta^r|$ they behave as expected, i.e. forming approximately horizontal lines for KAM circles.

2.4 Numerical analysis of resonance growth

The aim of this section is to describe the method and results of our numerical analysis. To study the growth of resonances, one must first design a scheme to choose the values of other integrals for different spins. A good guide is again the effective potential. Our goal is that the energy and angular momentum allow for plunging orbits, as this is suggested by some works (see, e.g., [30]) to make non-linear behavior more prominent even for a resonance enclosed by an KAM circle; also, we defined the AA-like variables in such a way that we require the existence of an unstable point near the left tip of the main island of stability. To fulfill this criterion for small enough spins ($S \lesssim 10^{-1}\,\mu M$), we simply choose a value for J_z and take the value of the geodesic effective potential at its local maximum (corresponding to an unstable circular equatorial geodesic orbit) as the energy, which we will keep the same for different spin values. Typically, the effective potentials will then look as in Fig. 2.3. We then use a program (see A.2) to search for the given resonance along the $r = 0$ line and after locating the

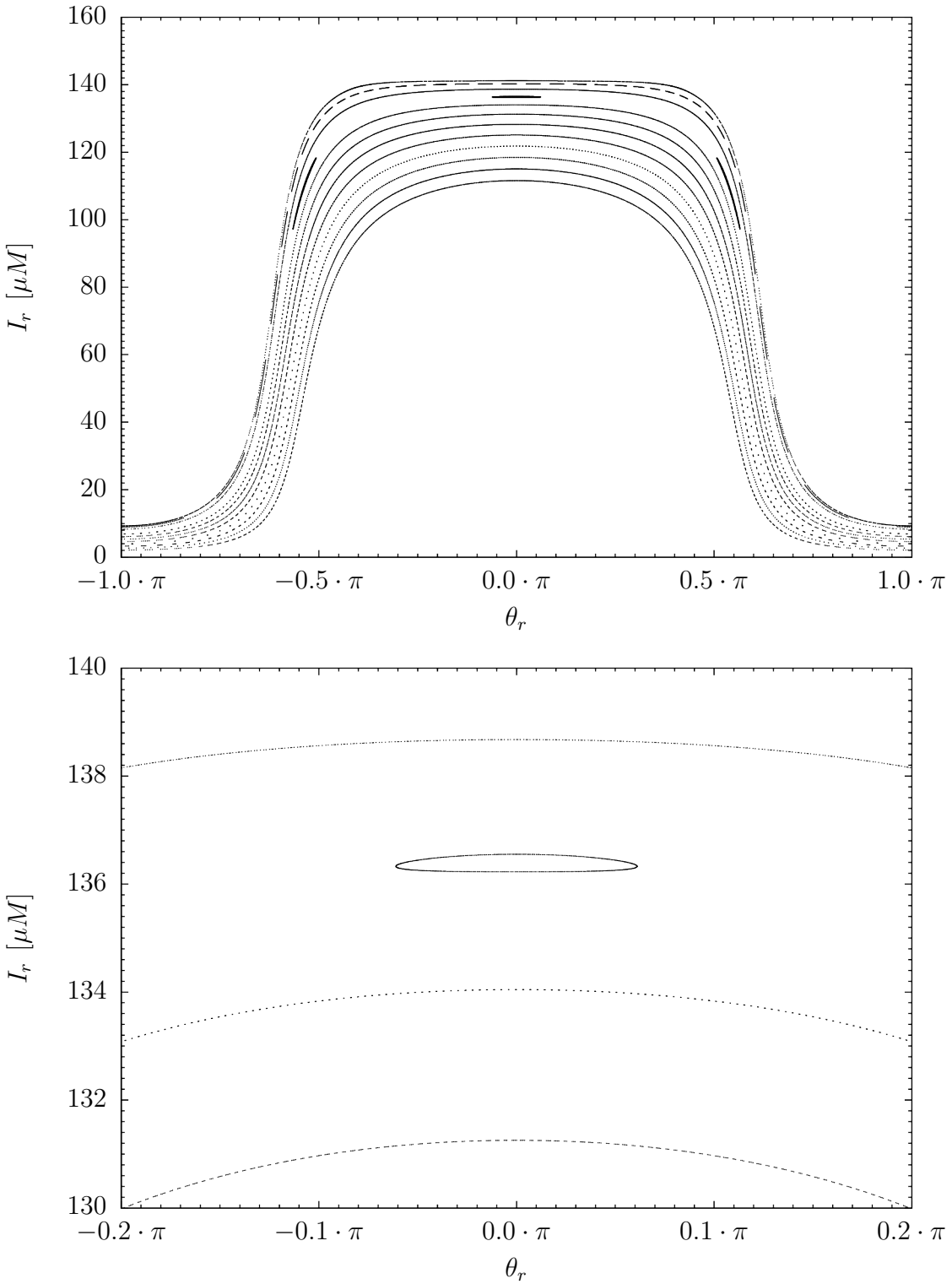

Figure 2.2: Data from the surface of section in Fig. 1.3 converted to AA-like variables. Top panel: full surface of section, bottom panel: zoom at the 1/3 island.

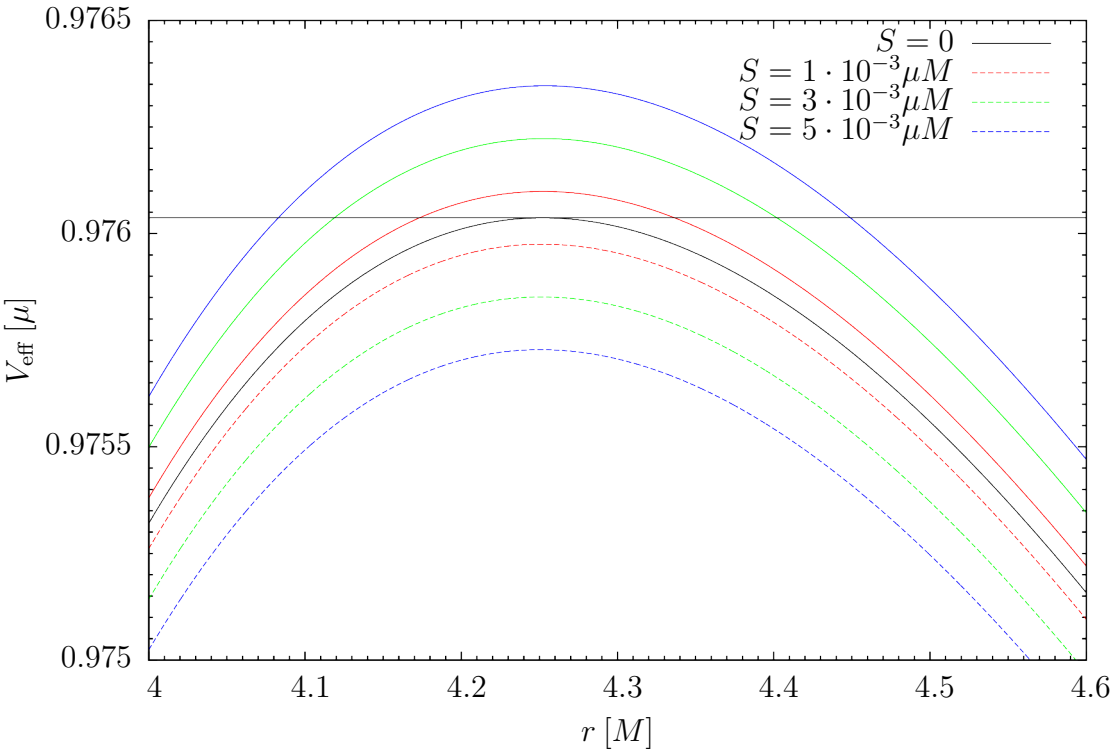

Figure 2.3: Shapes of the effective potential for low spin values near the unstable point. Black lines show the geodesic effective potential and the corresponding energy level of the circular equatorial unstable orbit at $E \doteq 0.976\,037\mu$. Coloured lines show the effective potential for non-zero spin; full lines correspond to $V_{\text{eff}(+)}$ and dashed lines to $V_{\text{eff}(-)}$.

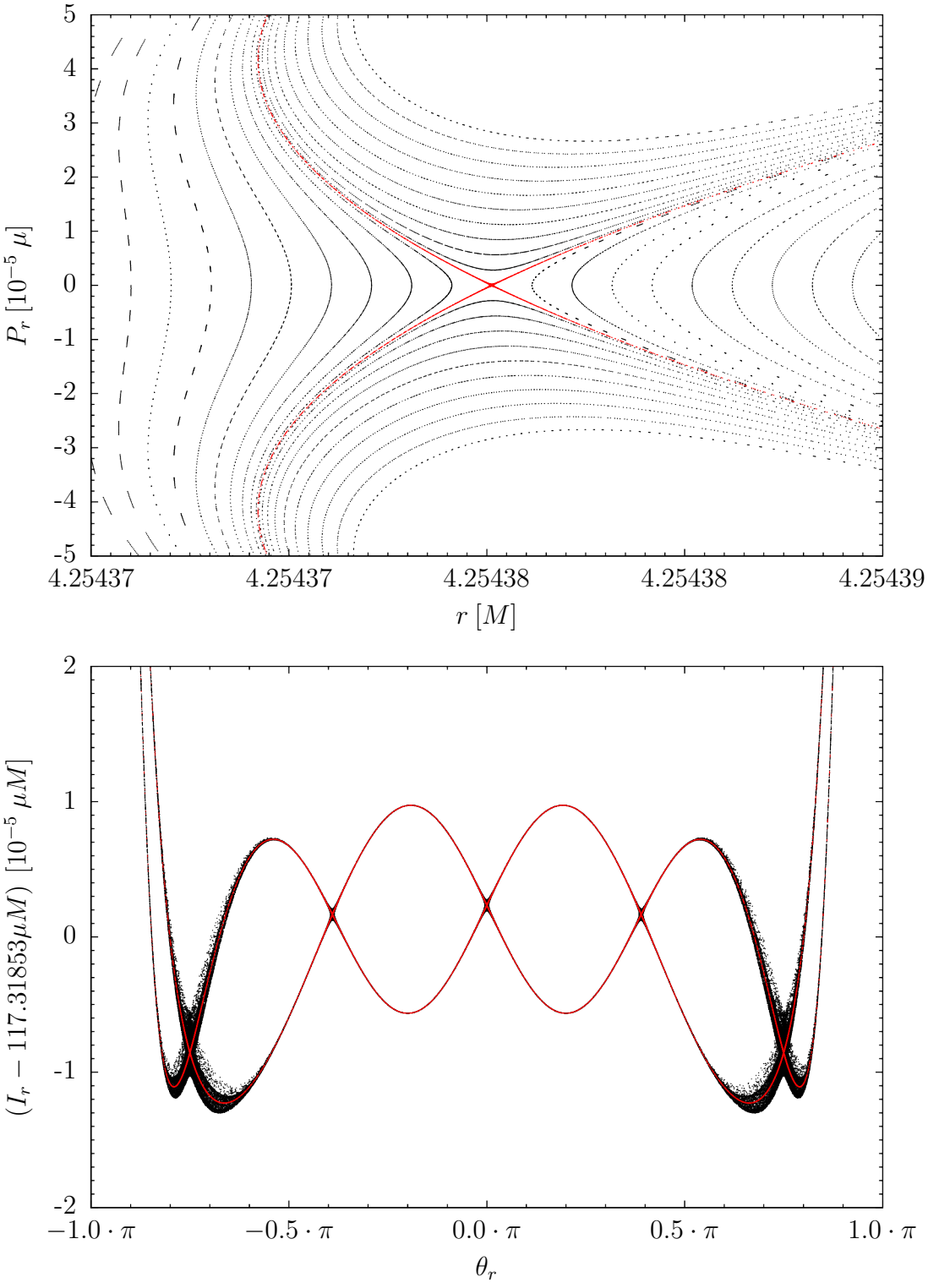

Figure 2.4: Top panel: Surface of section for $E \doteq 0.976\,037\mu$, $J_z = 3.8\mu M$, $S = 10^{-3}\ \mu M$ showing the 2/3 resonance; separatrix is shown in red, black lines left and right of the separatrix are KAM curves, above and under are in the resonant islands of stability. Bottom panel: top panel converted to AA-like variables.

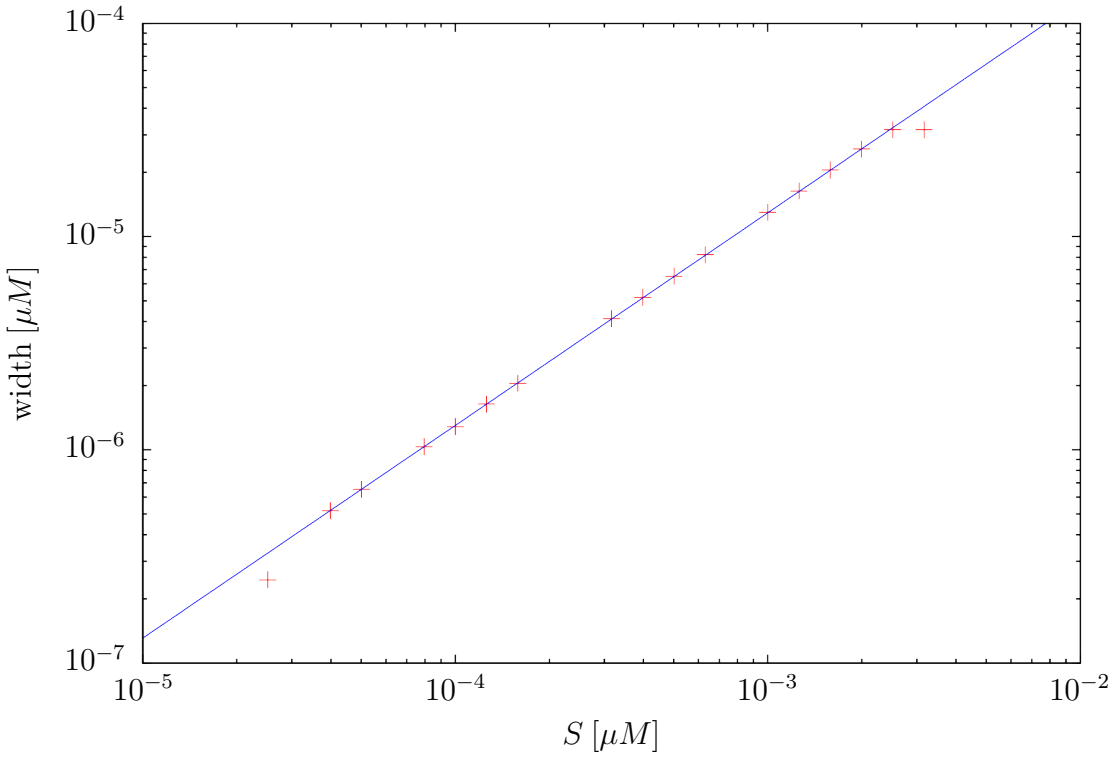

Figure 2.5: Growth of resonance 2/3.

separatrix, the angle at which it opens is measured and the resonance width is calculated.

The growth of the 2/3 resonance with $J_z = 3.8\mu M$ was investigated by taking 31 different values of the spin distributed geometrically in the interval $[10^{-5}\,\mu M, 10^{-2}\,\mu M]$ and the procedure above was applied to measure the width of the 2/3 resonance at the left tip of the main island of stability. Eq. (2.11) was used to estimate the width of the resonance with parameters $s = 3$, $n = 2$. The result is shown in Fig. 2.5, where the blue line corresponds to a fit of the function

$$\log \frac{\text{width}}{\mu M} = A + q \cdot \log \frac{S}{\mu M}\,, \tag{2.14}$$

to the measured points except for the leftmost and rightmost ones, which was performed in logscale without taking errors of separatrix width measurement into account and returned the values

$$A = -4.366 \quad \pm 0.013\,, \tag{2.15a}$$
$$q = \quad 0.9974 \pm 0.0016\,. \tag{2.15b}$$

This shows that the resonance width grows linearly with spin. Recall that the resonance grows as the square root of the relevant perturbation (see Sec. 2.2); we can thus conclude that the growth of the 2/3 resonance is driven by the second-order in spin terms.

3. Gravitational waveforms

3.1 Weyl tensor

The Weyl tensor $C_{\mu\nu\rho\sigma}$ is the traceless part of the Riemann curvature tensor $R_{\mu\nu\rho\sigma}$, i.e. terms composed solely of the metric $g_{\mu\nu}$, the Ricci tensor $R_{\mu\nu} = R^{\alpha}{}_{\mu\alpha\nu}$ and the scalar curvature $R = R^{\mu}{}_{\mu}$ are subtracted from the Riemann tensor so as to achieve

$$C^{\alpha}{}_{\mu\alpha\nu} = 0\,. \tag{3.1}$$

While in dimension 2 it is identically zero, in higher dimensions this is not the case. Since the mass-energy tensor $T_{\mu\nu}$ and its trace T directly determine the Ricci tensor and the scalar curvature through the Einstein equations as $R = -8\pi g^{\rho\sigma}T_{\rho\sigma}$, $R_{\mu\nu} = 8\pi\left(T_{\mu\nu} - g^{\rho\sigma}T_{\rho\sigma}g_{\mu\nu}/2\right)$, the Weyl tensor represents the curvature not directly connected to matter. The explicit form in spacetime dimension 4 is

$$\begin{aligned} C_{\mu\nu\rho\sigma} = R_{\mu\nu\rho\sigma} &+ \frac{1}{2}\left(R_{\mu\sigma}g_{\nu\rho} - R_{\mu\rho}g_{\nu\sigma} + R_{\nu\rho}g_{\mu\sigma} - R_{\nu\sigma}g_{\mu\rho}\right) \\ &+ \frac{1}{6}R\left(g_{\mu\rho}g_{\nu\sigma} - g_{\mu\sigma}g_{\nu\rho}\right)\,. \end{aligned} \tag{3.2}$$

The Weyl tensor inherits the basic symmetries of the Riemann tensor, namely:

$$C_{\mu\nu\sigma\rho} = C_{\nu\mu\rho\sigma} = -C_{\mu\nu\rho\sigma}\,, \tag{3.3a}$$

$$C_{\mu[\nu\sigma\rho]} = 0\,. \tag{3.3b}$$

The Riemann tensor has 20 independent components, by removing the 10 independent components of the Ricci tensor, one gets 10 independent components of the Weyl tensor.

3.2 Newman-Penrose formalism

The NP formalism is a parametrization of spacetime properties using a null tetrad and its corresponding components of relevant tensor quantities. We only provide the most elementary information, for more, see [31]. The basic building block of the Newman-Penrose formalism is a null tetrad l^{μ}, n^{μ}, m^{μ}, $\bar{m}^{\mu}$, which satisfies the following conditions:

$$l^{\mu}, n^{\mu} \in \mathbb{R}, \quad m^{\mu} \in \mathbb{C}\setminus\mathbb{R}\,, \tag{3.4a}$$

$$l_{\mu}l^{\mu} = n_{\mu}n^{\mu} = m_{\mu}m^{\mu} = \bar{m}_{\mu}\bar{m}^{\mu} = 0\,, \tag{3.4b}$$

$$l_{\mu}n^{\mu} = -1, m_{\mu}\bar{m}^{\mu} = 1\,, \tag{3.4c}$$

where $\bar{m}^{\mu}$ is the complex conjugate of m^{μ}.

In the NP formalism, 12 spin coefficients (tetrad components of covariant derivatives of tetrad fields), 7 Ricci-NP scalars and 5 Weyl-NP scalars (tetrad components of the Ricci and Weyl tensors, respectively) are defined. The Weyl-

NP scalars read

$$\psi_0 := C_{\mu\nu\rho\sigma} l^\mu m^\nu l^\rho m^\sigma \,, \tag{3.5a}$$
$$\psi_1 := C_{\mu\nu\rho\sigma} l^\mu n^\nu l^\rho m^\sigma \,, \tag{3.5b}$$
$$\psi_2 := C_{\mu\nu\rho\sigma} l^\mu m^\nu \bar{m}^\rho n^\sigma \,, \tag{3.5c}$$
$$\psi_3 := C_{\mu\nu\rho\sigma} n^\mu l^\nu n^\rho \bar{m}^\sigma \,, \tag{3.5d}$$
$$\psi_4 := C_{\mu\nu\rho\sigma} n^\mu \bar{m}^\nu n^\rho \bar{m}^\sigma \,. \tag{3.5e}$$

In this formalism, the Einstein equations form a complicated set of partial differential equations of scalar variables.

A great advantage of this formalism is the simple expression of gravitational wave strains: simple calculation in the transverse-traceless gauge shows that for a tetrad which for $r \to \infty$ reads

$$l = \frac{\partial}{\partial t} + \frac{\partial}{\partial r} \,, \tag{3.6a}$$
$$n = \frac{1}{2}\left(\frac{\partial}{\partial t} - \frac{\partial}{\partial r}\right) \,, \tag{3.6b}$$
$$m = \frac{1}{\sqrt{2}r}\left(\frac{\partial}{\partial \theta} + \frac{i}{\sin\theta}\frac{\partial}{\partial \phi}\right) \,, \tag{3.6c}$$

where the t, r, θ, ϕ asymptotically match a set of spherical-like coordinates (works in any asymptotically flat spacetime!), we can write $\psi_4 = \left(\ddot{h}_+ - i\ddot{h}_\times\right)/2$ (see e.g. [32]). This means that by considering a suitable tetrad, the gravitational wave strains can be expressed very easily using the Weyl-NP scalar ψ_4. In case one is also considering incoming gravitational waves, ψ_0 serves a similar purpose.

3.3 Teukolsky equation

For the development of this section, it is necessary that the Weyl tensor possess a certain algebraic quality called Petrov type D, which in the Schwarzschild spacetime it does. In principle it means that for the unperturbed Schwarzschild spacetime $\psi_i = 0 \quad \forall i \in \{0, 1, 3, 4\}$. For more information we refer the reader to other literature, e.g. [31].

The Teukolsky equation employs the NP formalism to describe perturbations of test fields in a Kerr background. For the purposes of this thesis, it will suffice to restrict ourselves to the Schwarzschild case; for the more general Kerr spacetime, the interested reader is referred to [33], [34].

The tetrad used to derive the Teukolsky equation is the Kinnersley tetrad, which in the Schwarzschild spacetime reads

$$l = \frac{1}{f}\frac{\partial}{\partial t} + \frac{\partial}{\partial r} \,, \tag{3.7a}$$
$$n = \frac{1}{2}\left(\frac{\partial}{\partial t} - f\frac{\partial}{\partial r}\right) \,, \tag{3.7b}$$
$$m = \frac{1}{\sqrt{2}r}\left(\frac{\partial}{\partial \theta} + \frac{i}{\sin\theta}\frac{\partial}{\partial \phi}\right) \,. \tag{3.7c}$$

When using this tetrad, the equation for ψ_4 attains the form of a "master equation"

$$\begin{aligned}\frac{r^2}{f}\frac{\partial^2\Psi}{\partial t^2} - \frac{1}{\sin^2\theta}\frac{\partial^2\Psi}{\partial\phi^2} - \left(\frac{1}{r^2 f}\right)^s \frac{\partial}{\partial r}\left[\left(r^2 f\right)^{s+1}\frac{\partial\Psi}{\partial r}\right] - \frac{1}{\sin\theta}\frac{\partial}{\partial\theta}\left(\sin\theta\frac{\partial\Psi}{\partial\theta}\right) \\ - 2s\frac{i\cos\theta}{\sin^2\theta}\frac{\partial\Psi}{\partial\phi} - 2s\left(\frac{M}{f} - r\right)\frac{\partial\Psi}{\partial t} + s\left(s\cot^2\theta - 1\right)\Psi = 4\pi r^2 T\,.\end{aligned} \tag{3.8}$$

The Ψ (master variable), T (source term) and s (spin weight) can have different values for various types of test fields: it is possible to describe electromagnetic perturbations using $s = \pm 1$ and neutrino perturbations with $s = \pm 1/2$. For gravitational perturbations, however, it is the value $s = \pm 2$ that does the trick.

Since we are interested in outgoing gravitational waves, we only want to consider the evolution of the ψ_4. The corresponding master variable is $\Psi = r^{-4}\psi_4$ with the spin weight $s = -2$ and the source term is a complicated linear combination of the stress-energy tensor components corresponding to the tetrad vectors n and $\bar{m}$.

The conventional way to solve this equation is in the frequency domain, in which it is fully separable (see, e.g, [35]). This approach is highly effective for a geodesic source, because it is sufficient to work with very few frequencies. In the case of more complicated dynamics, however, a time-domain approach is preferable. Due to the spacetime axisymmetry, the ϕ degree of freedom is still separable.

Since we are interested in the gravitational radiation at distances very large in comparison to M, the quantity of interest will be the strain h at null infinity $\mathcal{J}^+$. It can be decomposed as

$$h = \sum_{\ell=2}^{\infty}\sum_{\mathrm{m}=1}^{\ell} h_{\ell\mathrm{m}}\cdot\ {}_{-2}Y_{\ell\mathrm{m}}\left(\theta,\phi\right) \tag{3.9}$$

where ${}_sY_{\ell\mathrm{m}}\left(\theta,\phi\right)$ are the spin-weighted spherical harmonics with spin-weight s.

3.4 Results: generated waveforms

In this section, waveforms from trajectories depicted in Chapter 1 are computed using the Teukode (see Attachment A.3 or [34, 36]). The simulations were carried out on the Virgo cluster at the Astronomical Institute of the Czech Academy of Sciences and split into multiple processes using MPI; typically, the ρ-direction was kept as a whole and the division was done into 8, 16 or 32 processes along the θ-coordinate line.

In the calculations carried out for this thesis, the HH coordinates were used with $\Sigma = 10$. The time step was determined using the Courant-Friedrichs-Lewy condition with $C_{CFL} = 2$. For more details on the coordinate system and numerical method, see Attachment A.3. The waveforms shown are evaluated at null infinity $\mathcal{J}^+$, which here corresponds to $\rho = \Sigma = 10$, in the equatorial plane $\theta = \pi/2$.

Fig. 3.1 shows the $\mathrm{m} = 1, 2, 3$ waveform computed using 2001×101 grid from a trajectory in the chaotic sea in Fig. 1.4. The orbit has eccentricity

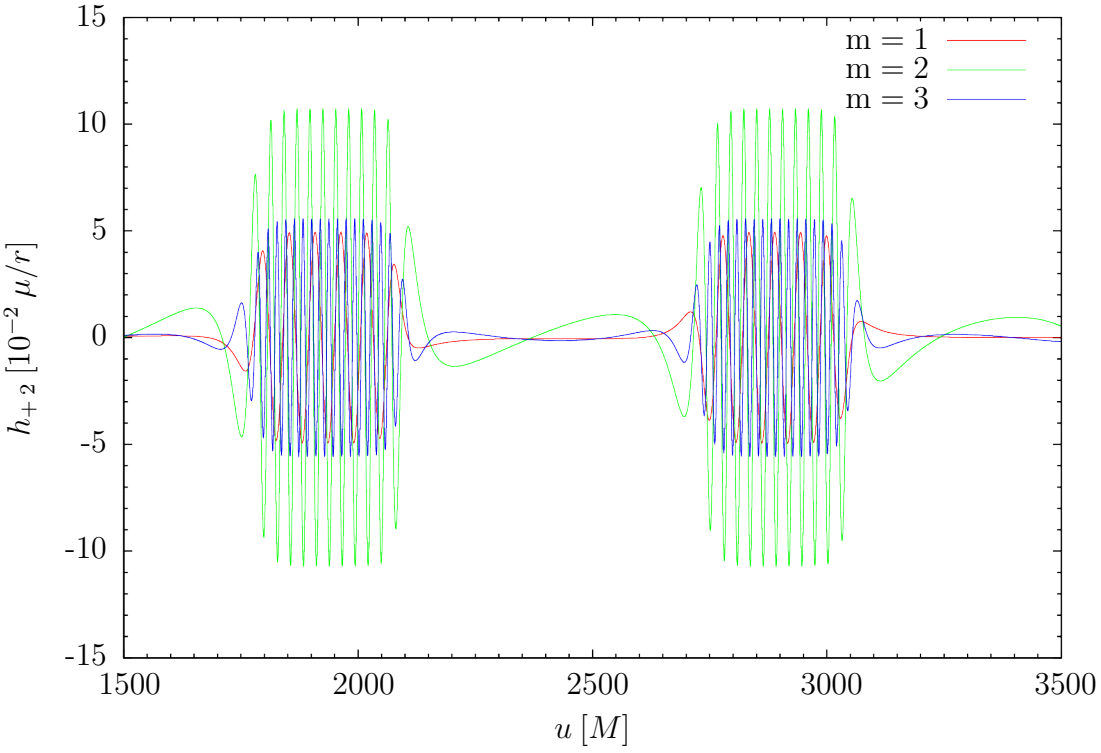

Figure 3.1: Waveform from a trajectory from the chaotic sea in Fig. 1.4 with initial $r = 4.25216M$ and $P_r = 0$, modes $\mathrm{m} = 1, 2, 3$.

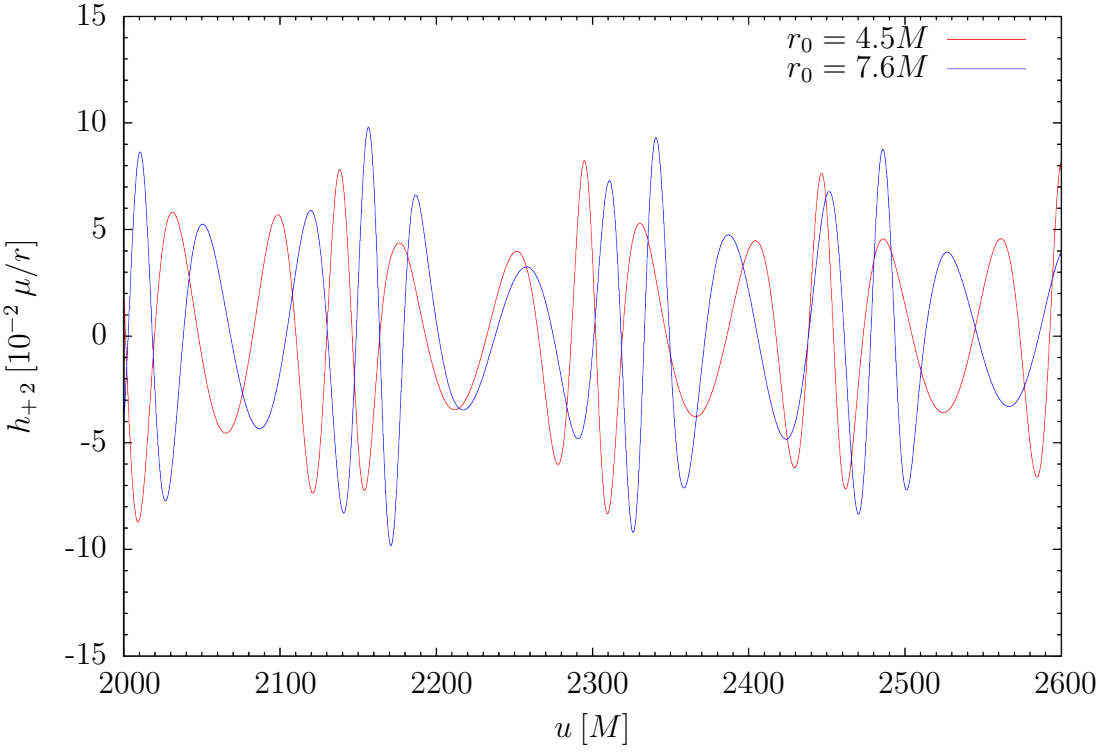

Figure 3.2: Waveforms of trajectories from Fig. 1.5, mode $\mathrm{m} = 2$.

$e \approx (r_{\max} - r_{\min}) / (r_{\max} + r_{\min}) \doteq 0.776$ and gets very close to the unstable orbit: $r_{\min} - r_{\text{upo}} \doteq 5.3 \cdot 10^{-5}\, M$. The waveform has the shape we expect from an EMRI (see, e.g., [37]).

Fig. 3.2 shows the m = 2 waveforms computed using a 1201×61 grid from both trajectories shown in Fig. 1.5. We can see that even in this highly perturbed case, a simple visual inspection is insufficient to distinguish whether the original orbit was regular or chaotic. We propose and apply a solution in the next chapter.

4. Recurrence analysis

4.1 Recurrence plots

Recurrence analysis is a method which allows us to analyze dynamics of regular and chaotic systems. It can be used to estimate dynamical invariants, such as the second-order Rényi entropy and correlation dimension, to uncover features such as unstable periodic orbits and sticky orbits, or simply to distinguish linear and non-linear behavior. For more detailed information on recurrence analysis, including different metrics to quantify the recurrence plots for a more substantial analysis of time series, see [38].

All we require is a time series in the full phase space $\vec{x}_i$. We define the recurrence matrix as

$$\mathbf{R}_{ij} = \begin{cases} \theta\left(\varepsilon - ||\vec{x}_i - \vec{x}_j||\right) & i \neq j \\ 0 & i = j \end{cases} , \tag{4.1}$$

where θ is the Heaviside step function and ε is a free parameter called the recurrence threshold. Intuitively, this simply means: $\mathbf{R}_{ij} = 1 \Leftrightarrow$ there is a recurrence at times i and $j \Leftrightarrow \vec{x}_i$ and $\vec{x}_j$ are closer than a given (small) threshold. The recurrence matrix is by definition symmetric. The main diagonal $i = j$ is excluded for technical reasons [38]. There is also an implicit ambiguity in the choice of metric. We define the recurrence rate (RR) as the density of ones in the recurrence matrix, for a time series of length l:

$$\mathrm{RR} = \frac{1}{l^2} \sum_{i,j=1}^{N,N} \mathbf{R}_{ij} \, . \tag{4.2}$$

Often, a specific value of RR (typically RR $\in [1\%, 5\%]$) is chosen and the threshold ε is then tuned to fit the given RR.

We can visualize this matrix by making a graph with the two axes i and j or, more practically, the times t_i and t_j, and plotting points for ones in the recurrence matrix. This is called a recurrence plot (RP).

Recurrence plots can be inspected visually to see some of the basic dynamical features, namely to distinguish linear and non-linear behavior. When a time series is quasiperiodic, there is a delay after which one finds recurrences for a sufficiently high recurrence threshold; i.e. $\forall i \; \mathbf{R}_{i,i+\Delta i} = 1$. This forms lines parallel to the main diagonal offset by Δi either in the horizontal or in the vertical direction.

In contrast, for a chaotic orbit, this regular structure only exhibits itself due to stickiness, a phenomenon where a chaotic orbit approaches an island of stability and mimics its regular behavior for a long period of time in interval I. The part of RP in the region $I \times I$ is formed by diagonal-parallel lines and forms a regular-looking square lying on the main diagonal. Furthermore, if the orbit is in a sticky regime in the intervals I_1 and I_2, then the region $(I_1 \times I_2) \bigcup (I_2 \times I_1)$, which shows correlations between the intervals I_1 and I_2, can either show a similar structure again if the orbit moves near the same island during both intervals or be empty if the two islands are different. This forms the typical square-like structure of a recurrence plot. Examples are shown in Fig.4.1, where we applied recurrence

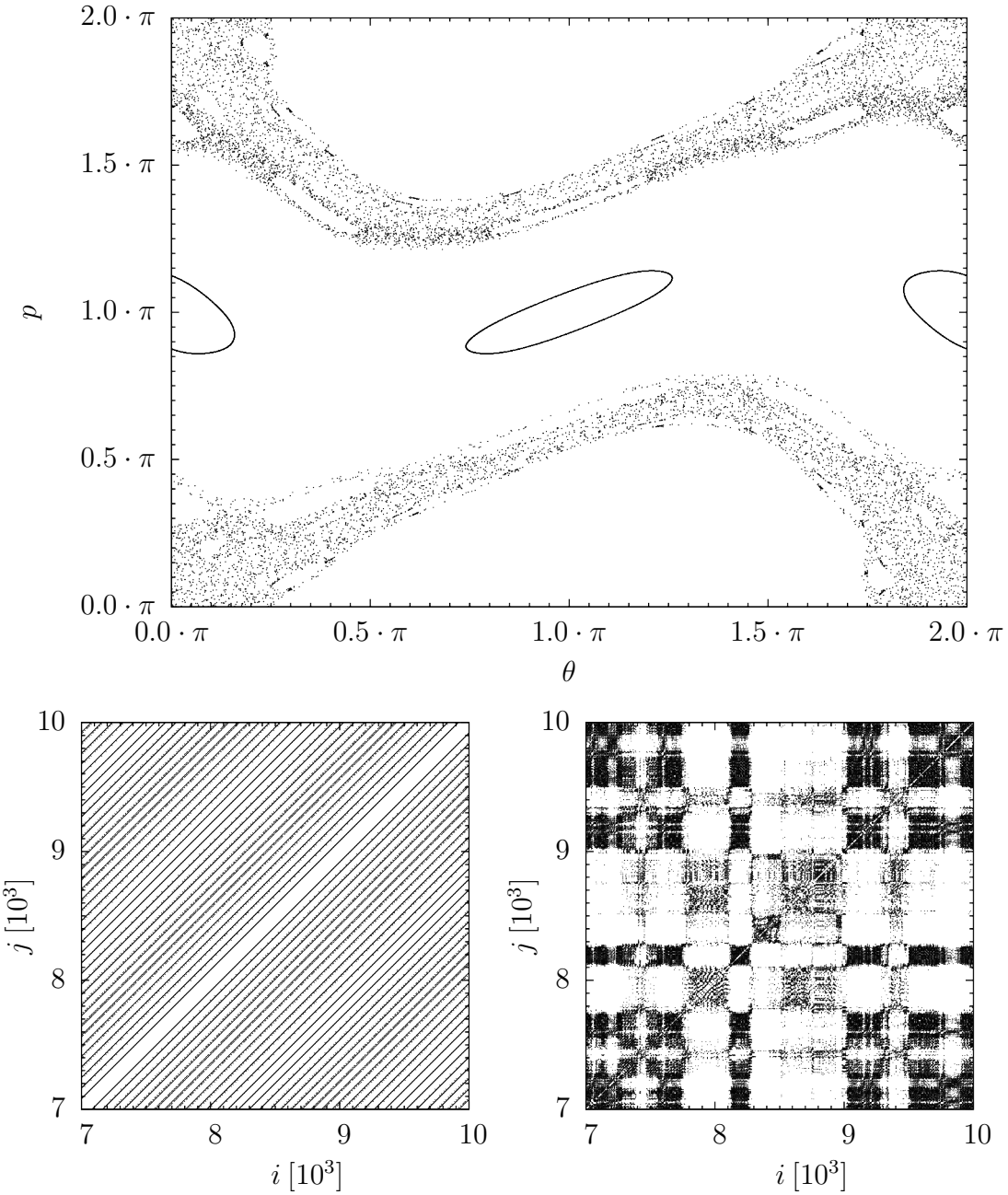

Figure 4.1: Top panel: Two trajectories of the Chirikov standard map for $K = 1$; bottom left panel: part of RP of the regular trajectory with initial conditions $\theta = \pi$, $p = \pi \cdot 92/99$, RR $= 0.01$; bottom right panel: part of RP of the chaotic trajectory with initial conditions $\theta = \pi$, $p = \pi \cdot 68/99$, RR $= 0.01$.

analysis to two trajectories of the Chirikov standard map [17]

$$\theta_{n+1} = \theta_n + p_{n+1} \,, \tag{4.3a}$$
$$p_{n+1} = p_n + K \sin \theta_n \tag{4.3b}$$

with the "kick" $K = 1$. It is a well-studied system, allowing us to demonstrate typical features of recurrence plots of regular and chaotic orbits.

4.2 Time delay method

The method as described above is powerful, but full phase space vectors are required. It can happen that we only have access to limited data (such as a simple scalar time series in a more complex system) and want to apply recurrence analysis; it is then necessary to use a phase space reconstruction technique. Here we describe the time delay method - usually also called embedding.

Let us have a time series $\vec{x}_i$ of dimension n_1 and length $l_1 \geq i \in \mathbb{N}$ in space $\mathcal{X}$. Let us also choose two free parameters: time delay $\mathcal{T} \in \mathbb{N}$ and embedding dimension $d \in \mathbb{N}$. We then call $\mathcal{X}^d$ the reconstructed phase space and define the reconstructed time series as

$$\vec{y}_i = \left(\vec{x}_i, \vec{x}_{i+\mathcal{T}}, ..., \vec{x}_{i+\mathcal{T}(d-1)}\right) \,, \tag{4.4}$$

which has dimension $n_1 \cdot d$ and is reduced in length to $l_1 - \mathcal{T}\,(d-1) = l_2 \geq i \in \mathbb{N}$. The trivial case without reconstruction is $d = 1$.

This method has been shown by [39] to provide a diffeomorphism between the original and reconstructed phase space under some conditions. This means that even using the data from a single suitable (i.e. not constant along the system's evolution) scalar function on the phase space we can still study the system's dynamics - in fact, this removes some of the ambiguity of the metric choice.

It is also necessary to make a suitable choice of parameters $\mathcal{T}$ and d. A suitable time delay is the first minimum of either the mutual information or the autocorrelation function. It is typical to then determine a suitable embedding dimension using the false nearest neighbor (FNN) method. The phase space is reconstructed using a given time delay $\mathcal{T}$ and embedding dimension d and for every point, the nearest point is found. It is considered a false nearest neighbor if their distance increases by a factor of at least f (we typically use $f = 5 - 10$) when the embedding dimension is changed to $d+1$. A suitable d is such that the fraction of FNNs is considered small enough.

An example is shown in Fig. 4.2 of RPs of both trajectories of Fig. 4.1; this time, however, only the θ variable was taken into account and the RPs were computed both with and without suitable embedding.

4.3 Recurrence plots of MPD orbits

We have applied recurrence analysis to MPD orbits. After several different attempts, we have come to the following method:

1. Sample the trajectory at a given rate in t to get a time series.

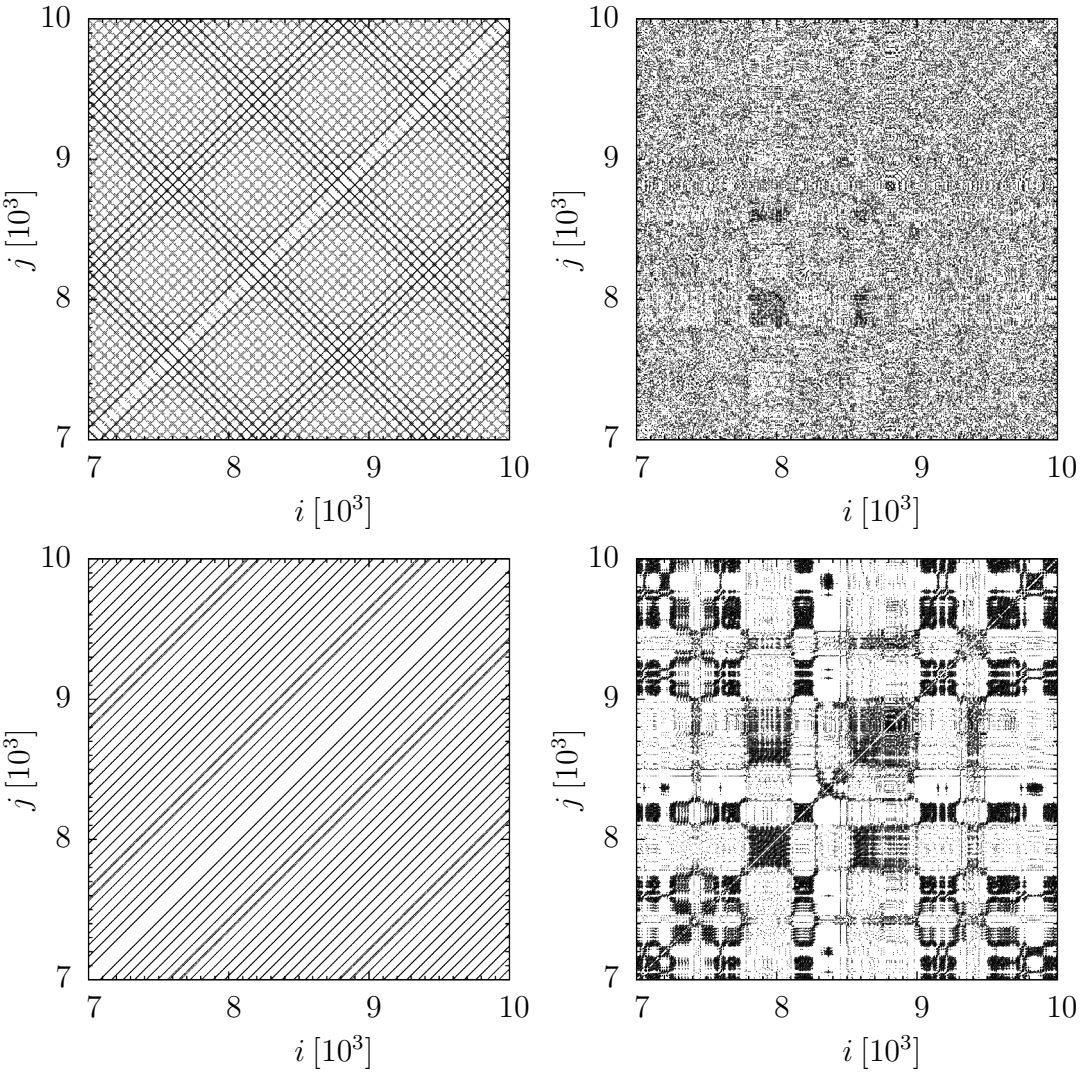

Figure 4.2: RPs of trajectories shown in Fig. 4.1 using only the θ variable, RR = 0.01; left: regular trajectory, right: chaotic trajectory; top: no embedding used, bottom: embedding dimension $d = 2$ with time delay $\mathcal{T} = 4$.

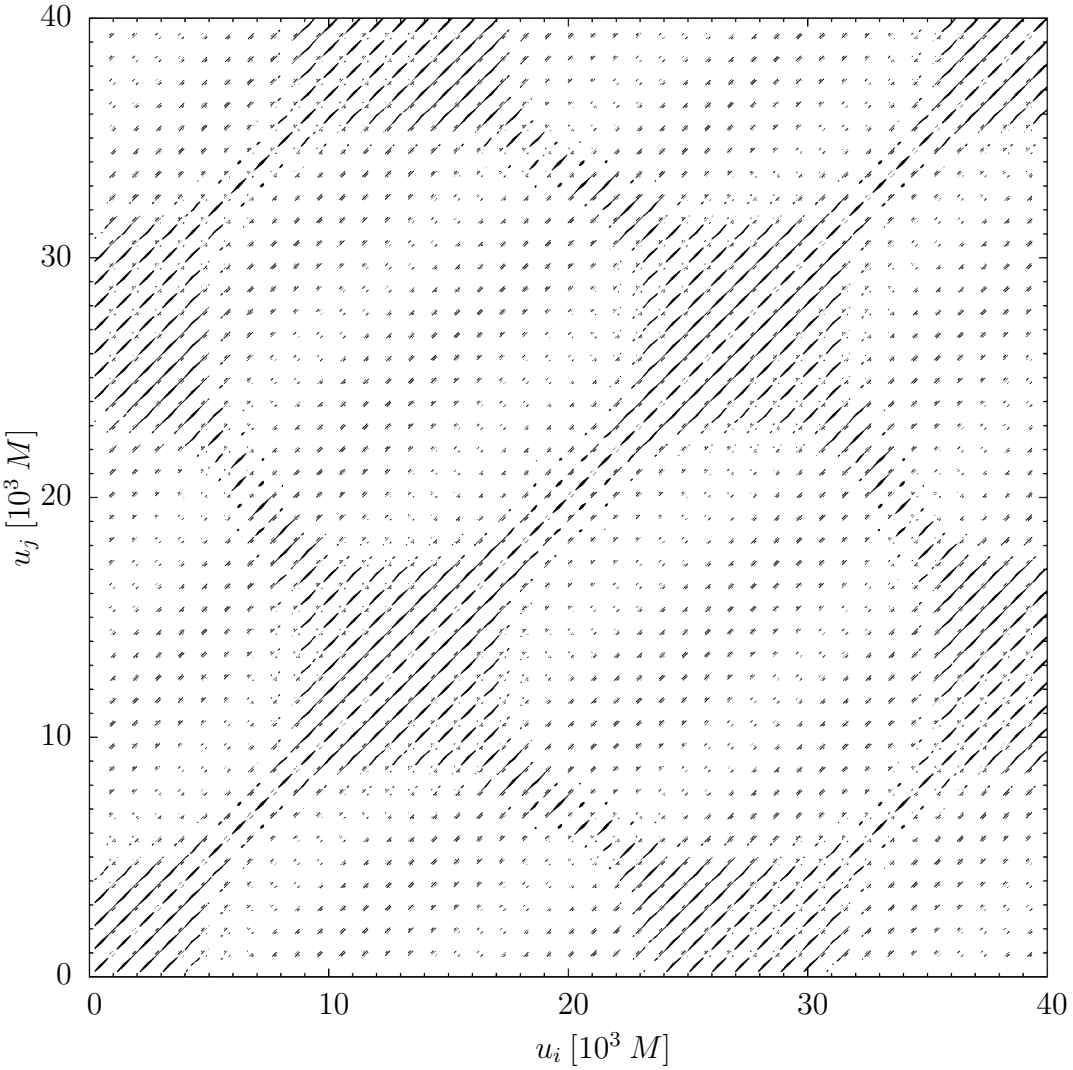

Figure 4.3: RP of a trajectory for $E = 0.97\mu$, $J_z = 3.8\mu M$, $S = 10^{-4}\,\mu M$ and initial $r = 4.25216M$ and $P_r = 0$. The orbit has been sampled at intervals of t of length $10.4M$ and the recurrence rate was chosen as RR $= 0.01$.

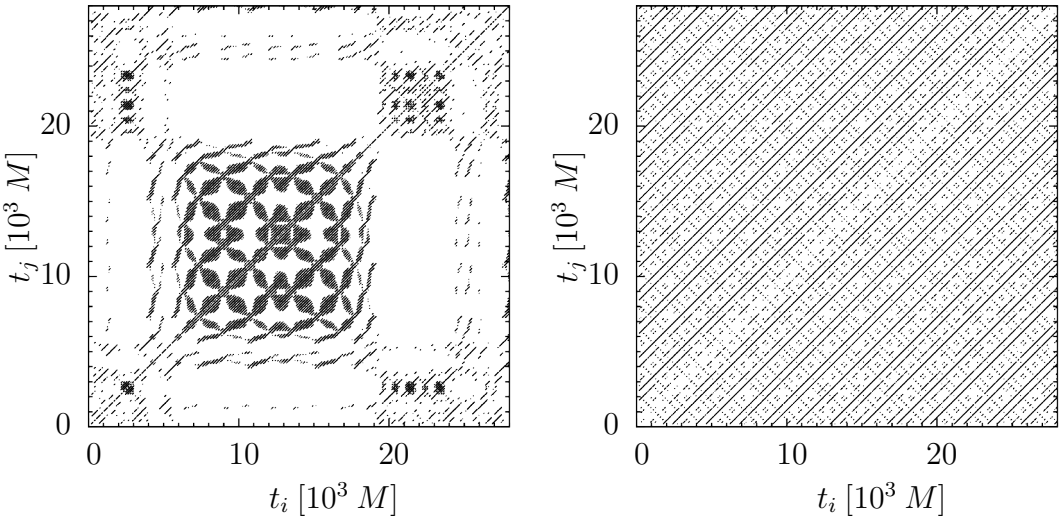

Figure 4.4: Recurrence plots of the trajectories of Fig. 1.5. The orbits have been sampled at intervals of t of length $8.667M$ and the recurrence rate was chosen as RR = 0.01.

2. Extract the data for r, θ, P_r, P_θ, and all four components of the spin vector $S^\mu = -\epsilon^{\mu\nu\kappa\lambda} P_\nu S_{\kappa\lambda}/2\mu$.

3. Normalize each of these time series to have zero mean and unit variance.

4. Choose a target value of RR.

5. Compute recurrence plot in the 8-dimensional space with the Euclidean metric; vary ε to reach the target RR.

This method has proven to give fairly clear recurrence plots in the high spin case. The t and ϕ degrees of freedom are irrelevant and therefore eliminated.

We have used the software `rp` developed by Norbert Marwan, see [40]. It computes the recurrence plot of a multivariate time series with or without embedding. It also computes the distribution of diagonal-parallel lines and derives some of the quantitative metrics.

A recurrence plot of an orbit with $S = 10^{-4}\,\mu M$ in the chaotic sea is shown in Fig. 4.3. By visual inspection, we see some of the characteristic chaotic features, but these are not very clear. On the other hand, Fig. 4.4 shows very clear recurrence plots of the trajectories for the spin value $S = 1.4\mu M$ depicted in Fig. 1.5.

4.4 Recurrence plots of gravitational waveforms

In this section, recurrence plots of waveforms calculated in the previous section are computed. These were made using the same software `rp` [40] as in the previous section.

In the case with $S = 10^{-4}\,\mu M$, we computed the recurrence plot using the information from all the three calculated m-modes. The waveform was sampled at

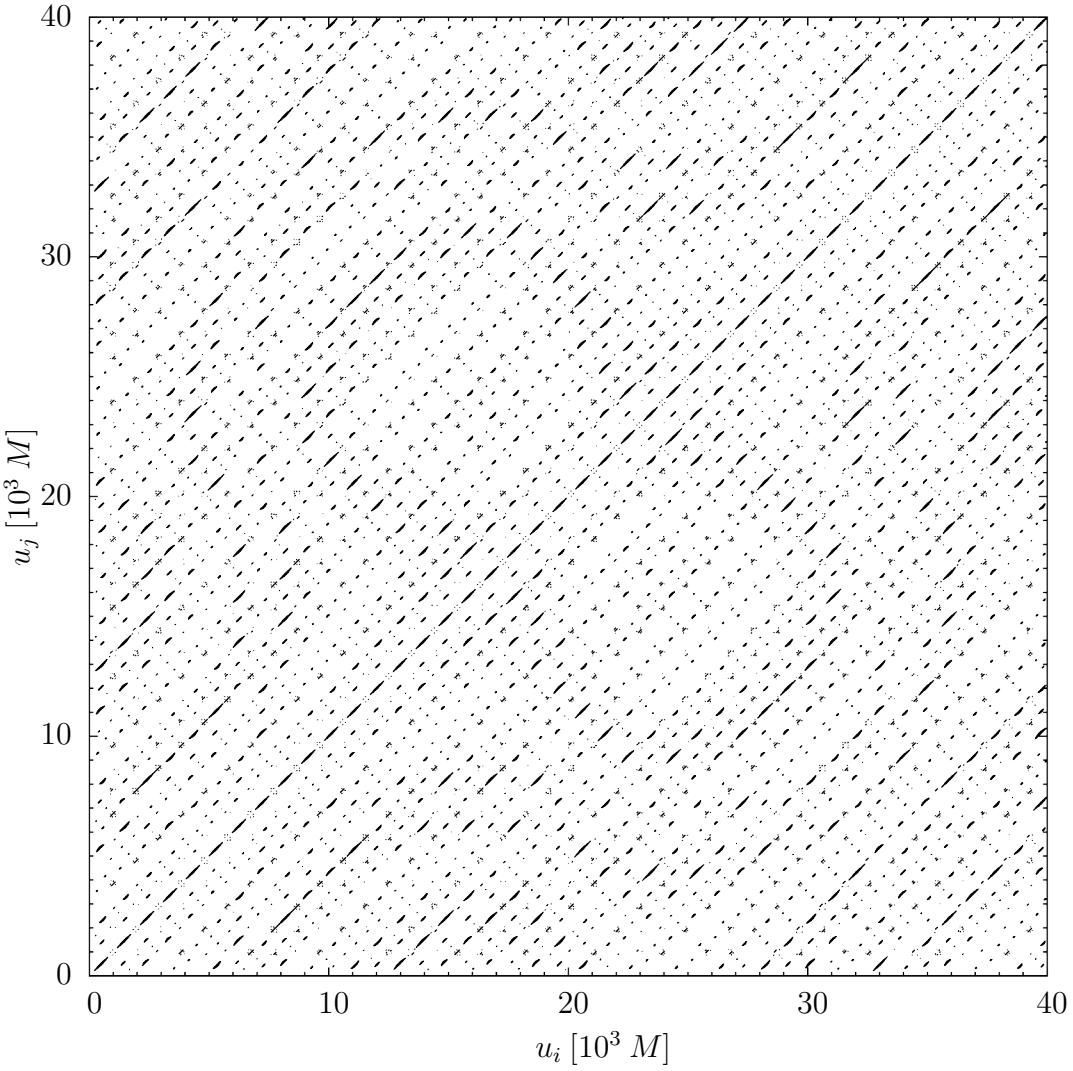

Figure 4.5: Recurrence plots of the waveforms of Fig. 3.1 sampled at intervals of $2.167M$ and the recurrence rate chosen as RR = 0.01.

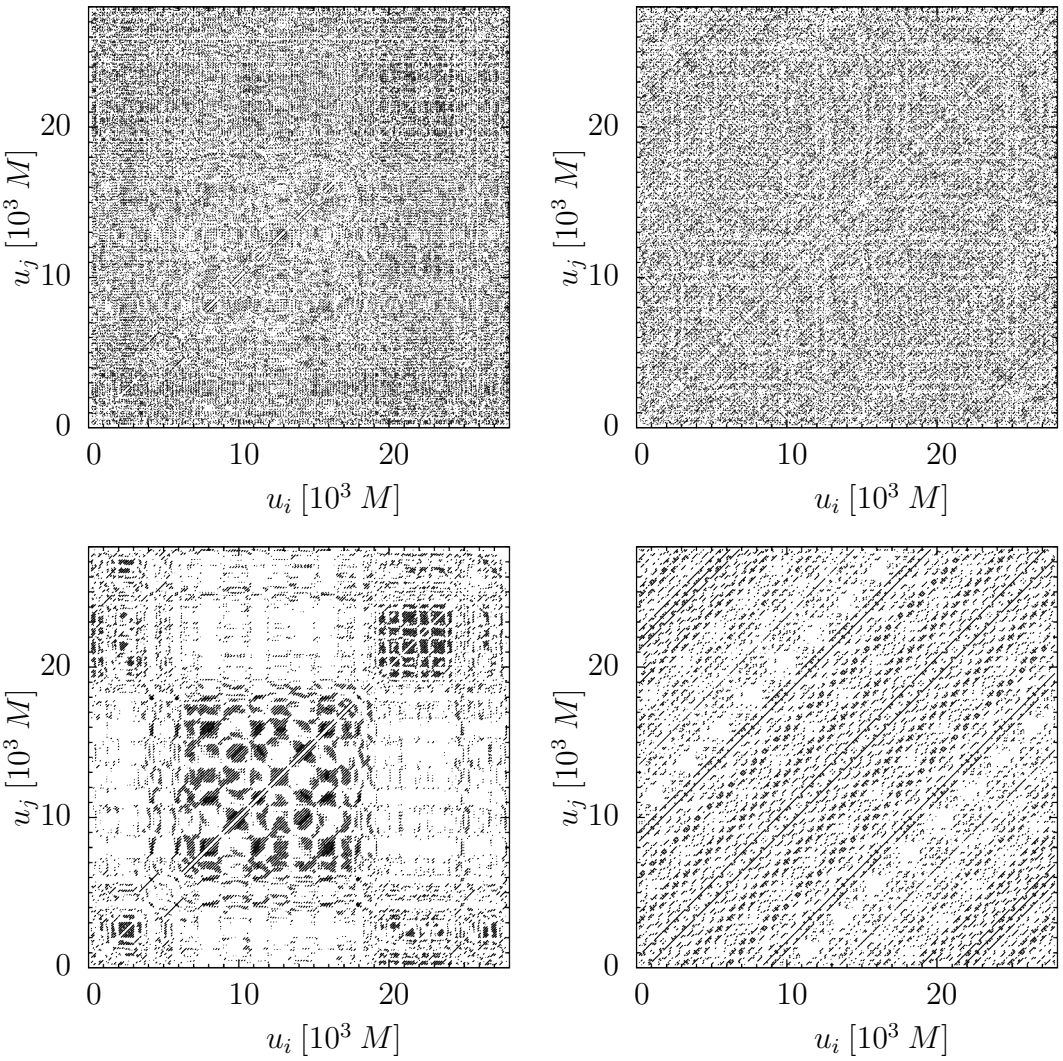

Figure 4.6: Recurrence plots of the waveforms of Fig. 3.2 sampled at intervals of $8.667M$ and the recurrence rate was chosen as RR $= 0.01$. Left is for the chaotic orbit, right is for the regular orbit. Top is without embedding, bottom is with time delay $\mathcal{T} = 1$ and embedding dimension $d = 21$.

intervals of $2.166M$ and the vectorial time series used for the RP was constructed as

$$(h_{+\,1}, h_{\times\,1}, h_{+\,2}, h_{\times\,2}, h_{+\,3}, h_{\times\,3})\,. \tag{4.5}$$

The false nearest neighbor algorithm then suggests that one does not require any embedding. This is in agreement with the expectation of being very close to the geodesic case, where the orbit is only described by two parameters. The resultant plot is shown in Fig. 4.5. In comparison to Fig. 4.3, one can see a little similarity, but this is very superficial and does not cover any actual dynamical features.

In the case of $S = 1.4\,\mu M$, only the + polarization of the waveform's m = 2 mode was used. The waveform was sampled at intervals of $8.667M$. Recurrence plots were computed both without embedding and with embedding with time delay $8.667M$ and embedding dimension $d = 21$ and are shown in Fig. 4.6. In comparison to Fig. 4.4, we see that the waveforms retain those dynamical features which are detectable using recurrence plots.

Thus, we can conclude that chaos remains encoded in the gravitational waveforms radiated from Extreme Mass Ratio Inspirals. In the weakly chaotic low spin case, however, it is naturally harder to detect and even low noise can be an obstacle.

Conclusion

There are two principal parts of this thesis. The first concerns the core of the system's dynamics and the second focuses on the outgoing gravitational waves.

In the first part, we have summarized the basics of near-integrable dynamical systems, chaos and applications in describing the motion of a spinning particle in the Schwarzschild spacetime background as a model for an Extreme Mass Ratio Inspiral (EMRI). We have developed Fortran codes to evolve the orbits of spinning particles and used them to see that chaos manifests itself even for spin values relevant to real astrophysical events. We have also designed a method of studying any resonance for any kind of perturbation of the conventional geodesic model in the Schwarzschild spacetime.

It is known that the inclusion of spin in the equations of motion causes the system to lose integrability [25]; however, due to the existence of approximate constants of motion [28], it is not yet clear whether this means that there are no prolonged resonances at linear order. This work shows that the 2/3 resonance is related to the second-order in spin terms and does not manifest itself at linear order in spin in the Schwarzschild spacetime. Thus, we have provided evidence that these terms do not cause the emergence of chaos, which in turn has little effect on the overall dynamics of an EMRI with a non-spinning supermassive black hole.

This result supports the expectation that spin-induced chaos and resonances will not play a significant role in EMRIs. Our work provides numerical evidence for the case of a single resonance. A more thorough sweep of the phase space should take place in the future. It is of interest to see whether other resonances display the same behavior and, most importantly, to extend this analysis to the Kerr spacetime to get a more complete picture of the dynamics of an EMRI.

In the second part of the thesis, we have described the Teukolsky equation, which corresponds to leading-order perturbations of the black hole spacetime. We have used the Teukode, a time-domain Teukolsky equation solver, to compute gravitational waveforms generated by the motion of a spinning particle in the Schwarzschild background. We have presented the basics of recurrence analysis and applied it to the waveforms.

Using recurrence plots, we have established a close link between dynamical features of the particle's motion and the corresponding gravitational waveforms with high enough spins. For low spins, however, we have to elaborate to confirm this connection. For example, one has to eliminate the numerical noise from the Teukode simulation. It would be of interest to repeat the simulations with a finer grid so as to see whether the reduced noise would contribute to a closer link between the orbit's and waveform's recurrence plots. Another problem that could be addressed is the nature of recurrence analysis, which is by design suited to systems with a finite number of degrees of freedom. Finally, a large challenge is the fact that the real signal will be heavily distorted by background and detector noise [26].

Even though recurrence analysis may not be able to detect spin-induced chaos in EMRIs, it could still be used to detect chaos from other sources. For example, chaos can occur due to a broken spacetime background symmetry, if the Kerr

hypothesis is incorrect (see, e.g., [26]) and prolonged resonances can occur due to the gravitational perturbation by the surrounding astrophysical environment [41].

Bibliography

[1] Weisberg, J. M., Taylor, J. H., and Fowler, L. A. (1981). Gravitational waves from an orbiting pulsar. Sci. Am., 245:66–74.

[2] Abbott, B. P. et al. (2016). Observation of gravitational waves from a binary black hole merger. Phys. Rev. Lett., 116(6):061102.

[3] Abbott, B. P. et al. (2018). Gwtc-1: A gravitational-wave transient catalog of compact binary mergers observed by ligo and virgo during the first and second observing runs. arXiv: 1811.12907.

[4] Babak, S., Gair, J., Sesana, A., Barausse, E., Sopuerta, C. F., Berry, C. P. L., Berti, E., Amaro-Seoane, P., Petiteau, A., and Klein, A. (2017). Science with the space-based interferometer LISA. V: Extreme mass-ratio inspirals. Phys. Rev., D95(10):103012.

[5] Klein, A. et al. (2016). Science with the space-based interferometer eLISA: Supermassive black hole binaries. Phys. Rev., D93(2):024003.

[6] Sesana, A. (2016). Prospects for Multiband Gravitational-Wave Astronomy after GW150914. Phys. Rev. Lett., 116(23):231102.

[7] Tamanini, N., Caprini, C., Barausse, E., Sesana, A., Klein, A., and Petiteau, A. (2016). Science with the space-based interferometer eLISA. III: Probing the expansion of the Universe using gravitational wave standard sirens. JCAP, 1604(04):002.

[8] Witzany, V., Steinhoff, J., and Lukes-Gerakopoulos, G. (2019). Hamiltonians and canonical coordinates for spinning particles in curved space-time. Class. Quant. Grav., 36(7):075003.

[9] Dixon, W. G. (1970a). Dynamics of extended bodies in general relativity. I. Momentum and angular momentum. Proc. Roy. Soc. Lond., A314:499–527.

[10] Dixon, W. G. (1970b). Dynamics of extended bodies in general relativity. II. Moments of the charge-current vector. Proc. Roy. Soc. Lond., A319:509–547.

[11] Dixon, W. G. (1974). Dynamics of extended bodies in general relativity. III. Equations of motion. Phil. Trans. Roy. Soc. Lond., A277:59–119.

[12] Mathisson, M. (1937). Neue mechanik materieller systemes. Acta Phys. Polon., 6:163–2900.

[13] Papapetrou, A. (1951). Spinning test particles in general relativity. 1. Proc. Roy. Soc. Lond., A209:248–258.

[14] Semerák, O. (1999). Spinning test particles in a Kerr field. 1. Mon. Not. Roy. Astron. Soc., 308:863–875.

[15] Lukes-Gerakopoulos, G. (2017). Time parameterizations and spin supplementary conditions of the Mathisson-Papapetrou-Dixon equations. Phys. Rev., D96(10):104023.

[16] J. Lichtenberg, A. and A. Lieberman, M. (1992). Regular and Chaotic Dynamics. Springer International Publishing, 2nd edition.

[17] Meiss, J. D. (1992). Symplectic maps, variational principles, and transport. Rev. Mod. Phys., 64:795–848.

[18] Morbidelli, A. (2002). Modern celestial mechanics: aspects of solar system dynamics. CRC Press, 1st edition.

[19] Lukes-Gerakopoulos, G. (2012). The non-integrability of the Zipoy-Voorhees metric. Phys. Rev., D86:044013.

[20] Henon, M. and Heiles, C. (1964). The applicability of the third integral of motion: some numerical experiments. Astron. J., 69:73–79.

[21] Voglis, N. and Efthymiopoulos, C. (1998). Angular dynamical spectra. A new method for determining frequencies, weak chaos and cantori. J. Phys. A: Math. Gen., 31:2913–2928.

[22] Ruelle, D. (1979). Ergodic theory of differentiable dynamical systems. Inst. Hautes Etudes Sci. Publ. Math., 50:27–58.

[23] Hartman, P. (1960). A lemma in the theory of structural stability of differential equations. Proc. Am. Math. Soc., 11:610–620.

[24] Suzuki, S. and Maeda, K.-i. (1997). Chaos in Schwarzschild space-time: The motion of a spinning particle. Phys. Rev., D55:4848–4859.

[25] Hartl, M. D. (2003). Dynamics of spinning test particles in Kerr space-time. Phys. Rev., D67:024005.

[26] Lukes-Gerakopoulos, G. and Kopáček, O. (2018). Recurrence Analysis as a tool to study chaotic dynamics of extreme mass ratio inspiral in signal with noise. Int. J. Mod. Phys., D27(02):1850010.

[27] Arnold, V., Kozlov, V., and Neishtadt, A. (2006). Mathematical Aspects of Classical and Celestial Mechanics. Springer International Publishing, 3rd edition.

[28] Rüdiger, R. and Penrose, R. (1981). Conserved quantities of spinning test particles in general relativity. I. Proc. Roy. Soc. Lond., A375:185–193.

[29] Witzany, V. (2019). Hamilton-Jacobi equation for spinning particles near black holes. submitted to Phys. Rev., D.

[30] Contopoulos, G., Harsoula, M., and Lukes-Gerakopoulos, G. (2012). Periodic orbits and escapes in dynamical systems. Celestial Mech., 113:255.

[31] O'Neill, B. (1995). The geometry of Kerr black holes. A.K. Peters, 1st edition.

[32] Shibata, M. (2016). Numerical Relativity. World Scientific, 1st edition.

[33] Teukolsky, S. A. (1973). Perturbations of a rotating black hole. 1. Fundamental equations for gravitational electromagnetic and neutrino field perturbations. Astrophys. J., 185:635–647.

[34] Harms, E., Bernuzzi, S., Nagar, A., and Zenginoglu, A. (2014). A new gravitational wave generation algorithm for particle perturbations of the Kerr spacetime. Class. Quant. Grav., 31(24):245004.

[35] Press, W. H. and Teukolsky, S. A. (1973). Perturbations of a rotating black hole. II. Dynamical stability of the Kerr metric. Astrophys. J., 185:649–674.

[36] Harms, E. (2016). Gravitational waves from black hole binaries in the point-particle limit. PhD thesis, Friedrich-Schiller-Universität, Jena.

[37] Drasco, S. and Hughes, S. A. (2006). Gravitational wave snapshots of generic extreme mass ratio inspirals. Phys. Rev., D73(2):024027. [Erratum: Phys. Rev.D90,no.10,109905(2014)].

[38] Marwan, N., Romano, M., Thiel, M., and Kurths, J. (2007). Recurrence plots for the analysis of complex systems. Phys. Rept., 438:237–329.

[39] Takens, F. (1981). Detecting strange attractors in turbulence. Lec. Notes Math., 898:366–381.

[40] Marwan, N. (2013). TOCSY - Commandline recurrence plots. `http://tocsy.pik-potsdam.de/commandline-rp.php`. Last checked on May 01, 2019.

[41] Bonga, B., Yang, H., and Hughes, S. A. (2019). Tidal resonance in extreme mass-ratio inspirals. arXiv: 1905.00030.

[42] Fujita, R. and Hikida, W. (2009). Analytical solutions of bound timelike geodesic orbits in Kerr spacetime. Class. Quant. Grav., 26:135002.

[43] Yang, H., Zimmerman, A., Zenginoğlu, A., Zhang, F., Berti, E., and Chen, Y. (2013). Quasinormal modes of nearly extremal Kerr spacetimes: spectrum bifurcation and power-law ringdown. Phys. Rev., D88(4):044047. [Phys. Rev.D88,044047(2013)].

List of Figures

A. Attachments

A.1 Analytic properties of geodesics

When considering geodesic motion in the Schwarzschild spacetime, the transformation between the coordinates (x^μ, P_ν) and the AA variables can be explicitly written using integrals, for full derivation see [42]. We only give the r-action and angle. They are given using the polynomial

$$R\left(r; E, J_z, \mathcal{C}\right) = \frac{E^2 r^4}{\mu^2} - r^2 f\left(r^2 + J_z^2 + \mathcal{C}\right) \tag{A.1}$$

as

$$I_r^{geo}\left(r; E, J_z, \mathcal{C}\right) = 2\int_{r_2}^{r_1} R^{1/2}\left(r'\right) \mathrm{d}r' \,, \tag{A.2a}$$

$$\theta_{geo}^r\left(r; E, J_z, \mathcal{C}\right) = \begin{cases} \pi \int_{r_2}^{r} R^{-1/2}\left(r'\right) \mathrm{d}r' \big/ \int_{r_2}^{r_1} R^{-1/2}\left(r'\right) \mathrm{d}r' & P_r \geq 0 \\ -\pi \int_{r_2}^{r} R^{-1/2}\left(r'\right) \mathrm{d}r' \big/ \int_{r_2}^{r_1} R^{-1/2}\left(r'\right) \mathrm{d}r' & P_r < 0 \end{cases} , \tag{A.2b}$$

where r_1 and r_2 are turning points; they are the highest and next-to-highest root of $R\left(r\right)$, respectively. The integrals are the energy E, the azimuthal component of the orbital angular momentum J_z and the Carter constant $\mathcal{C} = J_x^2 + J_y^2$ and their presence in R is implied. This way, the angle coordinate is defined with the convention $\theta_{geo}^r \in [-\pi, \pi]$.

The integrals in θ_{geo}^r can also be expressed using special functions, namely the incomplete elliptic integral of the first kind

$$F\left(\varphi, k\right) = \int_0^{\varphi} \frac{\mathrm{d}\vartheta}{\sqrt{1 - k^2 \sin^2 \vartheta}} = \int_0^{\sin\varphi} \frac{\mathrm{d}y}{\sqrt{\left(1 - y^2\right)\left(1 - k^2 y^2\right)}} \tag{A.3}$$

and the complete integral of the first kind $K\left(k\right) = F\left(\pi/2, k\right)$.

It is first necessary to find all the roots of $R\left(r\right)$ and rewrite as

$$R\left(r\right) = \left(1 - \frac{E^2}{\mu^2}\right)\left(r_1 - r\right)\left(r - r_2\right)\left(r - r_3\right) r, \quad 0 \leq r_3 \leq r_2 \leq r_1 \,. \tag{A.4}$$

Then we can express

$$\int_{r_2}^{r} R^{-1/2}\left(r'\right) \mathrm{d}r' = \frac{2}{\left(1 - E^2/\mu^2\right)\left(r_1 - r_3\right)\left(r_2 - r_4\right)} F\left(\arcsin y_r, k_r\right) \,, \tag{A.5}$$

where

$$y_r = \sqrt{\frac{r_1 - r_3}{r_1 - r_2}\frac{r - r_2}{r - r_3}} \,, \tag{A.6a}$$

$$k_r = \sqrt{\frac{r_1 - r_2}{r_1 - r_3}\frac{r_3 - r_4}{r_2 - r_4}} \,. \tag{A.6b}$$

Thus, the angle variable can be expressed as

$$\theta_{geo}^r = \begin{cases} \pi F(\arcsin y_r, k_r)/K(k_r) & P_r \geq 0 \\ -\pi F(\arcsin y_r, k_r)/K(k_r) & P_r < 0 \end{cases} . \tag{A.7}$$

The action variable, however, employs an integral for which there does not seem to be a closed form expression even using special functions.

To perform the conversion, we make use of Python 3 and the `numpy` and `scipy` libraries. More specifically, the function `scipy.integrate.quad` was used to compute the integral in Eq. (A.2a) and `scipy.special.ellipkinc` was used to evaluate the elliptic integral (Eq. (A.3)) in order to compute the angle variable in Eq. (A.2b).

A.2 Numerical solutions of the MPD equations

For numerical integration of orbits of spinning particles, a Fortran code was written named `MPD.for`. The input are values for initial r, P_r and integrals E, J_z and S; the code places a spinning particle with these parameters in the equatorial plane and calculates all the coordinate components of the four-momentum and the spin tensor using a Newton iteration method so as to satisfy the input values, $J_x = J_y = 0$, and the TD SSC. In this part, real variables are represented as quadruple precision floating point variables due to the ill-conditioned calculation of expressions such as $E + P_t$ and $J_z - P_\phi$.

Then it evolves the MPD equations using the Gauss collocation method of different orders using fixed-point iteration. Here, real variables are represented as double precision floating point. In this thesis, 4th order was used for all computations.

The code deals with the system as originally written in Eq. (1.2), i.e. x^μ, P_μ and $S^{\mu\nu}$; no reduction is applied for the integration. Thus, the integrals E, J_i, S^2, μ^2 and $P_\mu S^{\mu\nu}$ are used to track the integration error. In Fig. A.1, evolution of the relative error of energy is shown to be very low - on the order of 10^{-14}.

It also automatically writes the intersections with the Poincaré surface of section $\mathcal{S}$ using the evolution method's collocation polynomial and computes the rotation number using Eq. (1.19) for each initial condition. For n intersections (including the initial condition), the rotation number accuracy is

$$\Delta\nu_\vartheta = \frac{1}{n}. \tag{A.8}$$

Slightly different versions of the code were also used to locate the unstable periodic orbit (`MPD_upo.for`) and a given resonance (`MPD_src.for`) by evolving the equations of motion and using a bisection method to solve an equation employing a function of the initial r along the $P_r = 0$ line. In case of the `MPD_upo.for` code, the corresponding equation is $P_r = 0$ at the next intersection with $\mathcal{S}$. The code `MPD_src.for` attempts to find an initial r for which to find the desired rotation number. To make sure that the accuracy grows as the code converges, the number of iterations of the return mapping grows as well: if the two current estimates are $\omega_1 > \omega_2$, the next orbit is integrated long enough as to get $2/\min(\omega_1 - \omega_{target}, \omega_{target} - \omega_2)$ intersections.

To determine the width of a resonance p/q, Python 3 with the `numpy` and `scipy` libraries was used to fit

$$I_r = I_r^0 \pm \frac{\text{width} \cdot ns}{4}\theta^r \tag{A.9}$$

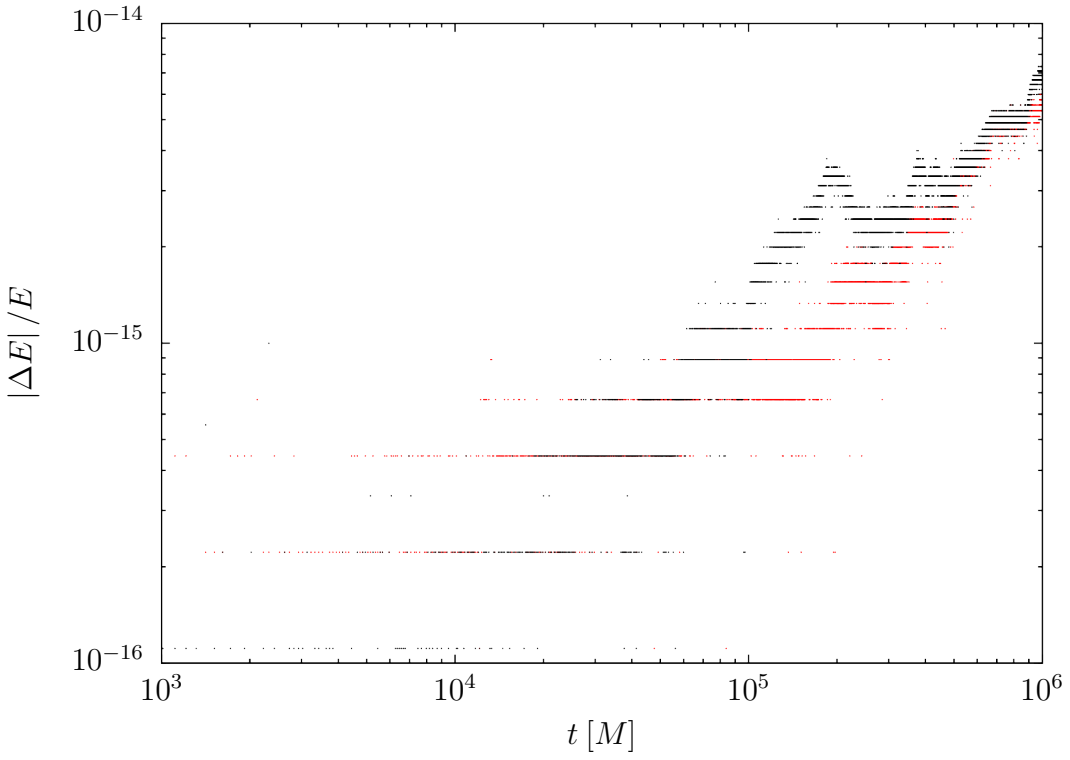

Figure A.1: Evolution of the relative error $\Delta E = |E(\tau) - E(0)|/E(0)$ for the trajectories of Fig. 1.5. Black points correspond to the regular trajectory, red points correspond to the chaotic trajectory.

to Poincaré section points (see Eq. (2.11)). Only points with $|\theta^r| < 0.01 \cdot 2\pi/(ns)$ were taken into account and as components of the vector of residuals we use

$$-I_r + I_r^0 + \text{sign}\left(I_r - I_r^0\right) \frac{\text{width} \cdot ns}{4} \theta^r \,. \tag{A.10}$$

This expression together with the function `scipy.optimize.least_squares` was used to estimate the values of I_r^0 and the width.

A.3 Teukode

A.3.1 Horizon-penetrating, hyperboloidal coordinates

The Teukode has been written in Jena as part of an MSc. thesis and the following dissertation [36]; for a more concise summary, see [34]. It is a time-domain solver for the master equation (3.8) with a point particle source. Different coordinate systems are used in the Teukode in order for the equation to be regular at the horizon and to smoothly reach the future null infinity $\mathcal{J}^+$. The system of choice is the horizon-penetrating, hyperboloidal (HH) coordinate system, see [43]. Here, its construction is described in the simpler Schwarzschild case.

The first step is to define

$$\tilde{t} = t + 2M \log|r - 2M| \,. \tag{A.11}$$

Then, one uses the technique of hyperboloidal compactification. The new variables Υ, ρ are defined by

$$\rho(r): \quad r = \frac{\rho(r)}{\Omega(\rho(r))}, \tag{A.12a}$$

$$\Upsilon\left(\tilde{t}, \rho\right) := t - h(\rho), \tag{A.12b}$$

where the h is called the height function and Ω the conformal factor. The choice made for them here is

$$\Omega(\rho) := 1 - \frac{\rho}{\Sigma}, \tag{A.13a}$$

$$h(\rho) := \frac{\rho}{\Omega} - \rho - 4M \log \Omega, \tag{A.13b}$$

where Σ is a free parameter and the location of $\mathcal{J}^+$ then corresponds to $\rho = \Sigma$. The position of the horizon is then

$$\rho_+ = \frac{2M\Sigma}{2M + \Sigma}. \tag{A.14}$$

A.3.2 Numerical solutions of the Teukolsky equation

The Teukode uses the HH coordinates to smoothly cover the whole region of interest from the horizon all the way to the null infinity $\mathcal{J}^+$. The equation is separated into m-modes by taking the Fourier transform in the ϕ-direction

$$\psi_4(\Upsilon, \rho, \theta, \phi) = \sum_{\mathrm{m}=-\infty}^{\infty} \Psi_{\mathrm{m}} e^{i\mathrm{m}\phi}, \tag{A.15}$$

the master equation (3.8) is then of the form

$$\begin{aligned} C_{\Upsilon\Upsilon}\partial_{\Upsilon\Upsilon}\Psi_{\mathrm{m}} + C_{\Upsilon\rho}\partial_{\Upsilon\rho}\Psi_{\mathrm{m}} + C_{\rho\rho}\partial_{\rho\rho}\Psi_{\mathrm{m}} + C_{\theta\theta}\partial_{\theta\theta}\Psi_{\mathrm{m}} + C_{\Upsilon}\partial_{\Upsilon}\Psi_{\mathrm{m}} \\ + C_{\theta}\partial_{\theta}\Psi_{\mathrm{m}} + C_{\rho}\partial_{\rho}\Psi_{\mathrm{m}} + C_0\Psi_{\mathrm{m}} = S_{-2}. \end{aligned} \tag{A.16}$$

The Teukode uniformly discretizes the interval $[\rho_+, \Sigma] \times [0, \pi]$ and implements different finite difference stencils up to 8th order to transform the reformulated 2+1 Teukolsky equation (A.16) into a set of ODEs; we used 6th order finite differencing. This is then evolved using a standard 4th order Runge-Kutta method. The step size is determined using the Courant-Friedrichs-Lewy (CFL) condition as $\Delta t = C_{CFL} \min\{h_\rho, h_\theta\}$, where the h_ρ and h_θ are the spacing in the ρ and θ direction, respectively, and $C_{CFL} \geq 1$. In this work, we use $C_{CFL} = 2$.

As an initial value problem, solving the Teukolsky equation requires initial conditions as well. Interference of the radiated waves from the previous ~ 2 orbits is quite important here, so we have chosen the simplest possible way: to use $\psi_4 = 0 \; \forall \rho, \theta$ and discard the first $\sim 200M$. The contrast of this beginning and later part is shown in Fig. A.2.

The source term is a complicated linear combination of the stress-energy tensor components. For a spinning particle, the stress energy tensor is only non-zero in a single point of the grid, represented by a δ function and its derivatives up to 3rd order. This is modeled using a narrow Gaussian approximation. For a

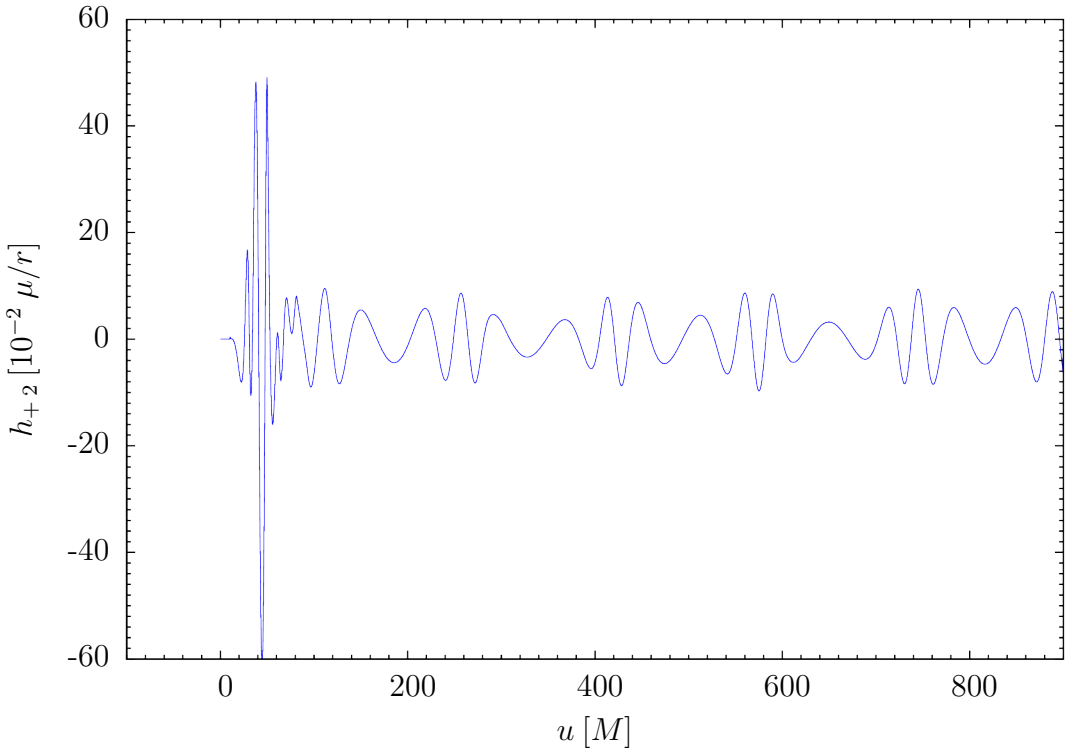

Figure A.2: Output of the initial $900M$ of the Teukode simulation corresponding to Fig. 3.2.

non-spinning particle source, the Teukode is also equipped with n-point delta approximations.

The Teukode also calculates energy and angular momentum fluxes. In the eccentric orbits presented here for $S = 10^{-4}\,\mu M$, the energy losses are $\dot{E} \doteq 10^{-3}\,\mu^2/M$ and angular momentum losses $\dot{J}_z \doteq 10^{-2}\,\mu^2$. This means that in our longest Teukode integration $t = 8.9 \cdot 10^4\,M$, assuming $\mu/M \doteq 10^{-4}$, we get a total relative energy loss $\Delta E/E \doteq 1\%$ and total relative angular momentum loss $\Delta J_z/J_z \cdot 2.3\%$.

Also, the advanced time v and retarded time u are defined as

$$u\,(t,r) := t - r_*\,, \tag{A.17a}$$

$$v\,(t,r) := t + r_*\,, \tag{A.17b}$$

$$r_*\,(r) := r + 2M \log\left(\frac{r}{2M} - 1\right)\,. \tag{A.17c}$$

Their meaning is that for an outgoing radial null geodesic (i.e. $\dot{\theta} = \dot{\phi} = 0$, $\dot{r} > 0$, $\mathrm{d}s^2 = 0$) u is a constant and only v changes along the geodesic - this makes u an ideal parameter for a waveform extracted at $\mathcal{J}^+$.

To check the calculation errors, we have run simulations with different grids on the same chaotic orbit as shown in Fig. 3.1. The waveform was calculated with grids 1201×61, 1701×141, 2401×201, 3401×281, 4801×401, 6801×561 and 9601×801; of these, the finest 9601×801 was taken as reference (closest to the exact solution, which we cannot get in any other way) and errors of the calculations with coarser grids were computed with respect to the reference grid.

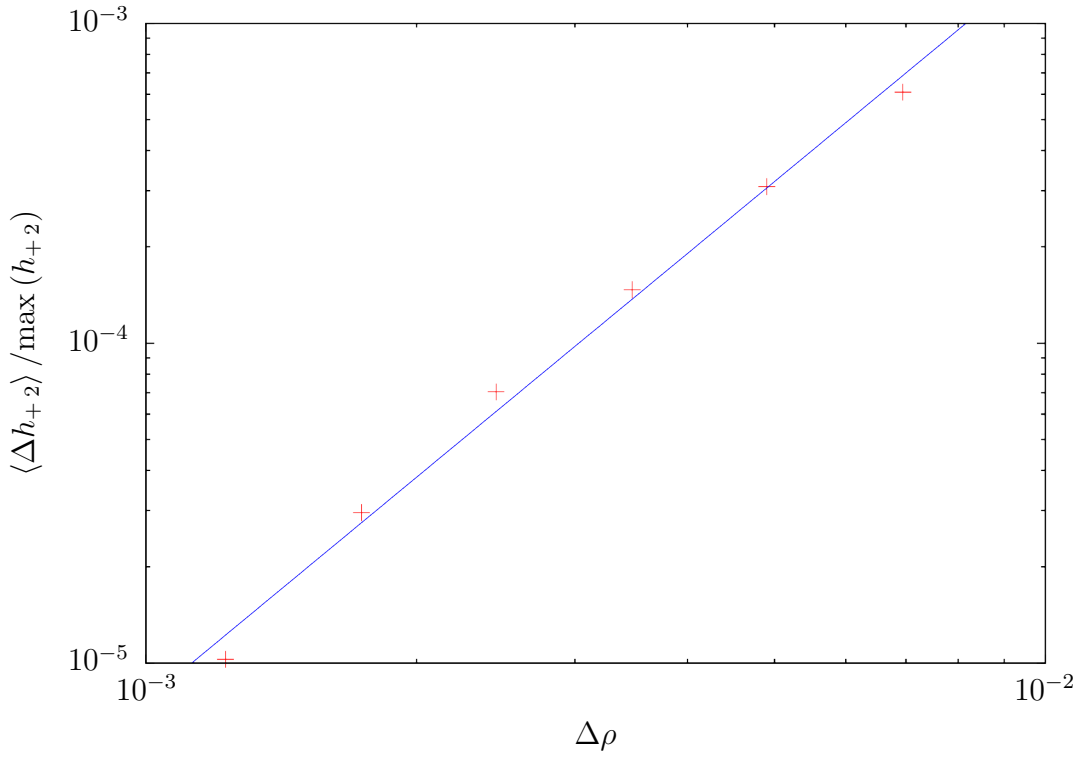

Figure A.3: Convergence plot of the Teukode.

We calculated the averaged absolute error

$$\left\langle \Delta h^{\mathrm{nx}}_{+\,2} \right\rangle = \frac{1}{50M} \int_{160M}^{210M} \left| h^{\mathrm{nx}}_{+\,2} - h^{9601}_{+\,2} \right| \mathrm{d}u \,, \tag{A.18}$$

where $h^{\mathrm{nx}}_{+\,2}$ is the + polarization of the m = 2 mode of the waveform calculated using nx points in the ρ direction distributed uniformly from the horizon at $\rho = 5/3$ and the null infinity $\mathscr{J}^+$ at $\rho = 10$, extracted at $\mathscr{J}^+$. The convergence plot is shown in Fig. A.3 with the grid spacing on the horizontal axis and the vertical axis showing the relative error with respect to the maximum of the reference waveform in the given interval.

The blue line corresponds to a fit of the function

$$\log \frac{\langle \Delta h_{+\,2} \rangle}{\max(h_{+\,2})} = A + q \cdot \log(\Delta\rho) \,, \tag{A.19}$$

which was performed in logscale and returned the values

$$A = 4.3 \quad \pm 0.6 \,, \tag{A.20a}$$

$$q = 2.32 \pm 0.09 \,. \tag{A.20b}$$

Since the evolution method used is 4th order, one would expect $q = 4$. However, the narrow Gaussian approximation for δ functions and their derivatives up to 3rd order is another source of error [36].